

The Deep SWIRE Field

II. 90cm Continuum Observations and 20cm–90cm Spectra

Frazer N. Owen,¹ G. E. Morrison,^{2,3} Matthew D. Klimek,^{1,4} & Eric W. Greisen,¹

ABSTRACT

We present one of the deepest radio continuum surveys to date at a wavelength $\gtrsim 1$ meter. The observations were taken with the VLA at 324.5 MHz covering a region of the SWIRE Spitzer Legacy survey, centered at $10^{\text{h}}46^{\text{m}}00^{\text{s}}$, $59^{\circ}01'00''$ (J2000). The data reduction and analysis are described and an electronic catalog of the sources detected above 5 sigma is presented. We also discuss the observed angular size distribution for the sample.

Using our deeper 20cm survey of the same field, we calculate spectral indices for sources detected in both surveys. The spectral indices for 90cm-selected sources, defined as $S \propto \nu^{-\alpha}$, shows a peak near 0.7 and only a few sources with very steep spectra, i.e. $\alpha_{20}^{90} \gg 1$. Thus no large population of very steep spectrum μJy sources seems to exist down to the limit of our survey.

For 20cm-selected sources, we find similar mean spectral indices for sources with $S_{20} > 1$ mJy. For weaker sources, below the detection limit for individual sources at 90cm, we use stacking to study the radio spectra. We find that the spectral indices of small ($< 3''$) 20cm-selected sources with $S_{20} < 10$ mJy have mean and median $\alpha_{20}^{90} \sim 0.3 - 0.5$. This is flatter than the spectral indices of the stronger source population. At the low end of the 20cm survey, the spectral indices appear to be steepening again.

We report $\log N - \log S$ counts at 90cm which show a flattening below 5 mJy. Given the median redshift of the population, $z \sim 1$, the spectral flattening and the flattening of the $\log N - \log S$ counts occurs at radio luminosities normally associated with AGN rather than with galaxies dominated by star-formation.

¹National Radio Astronomy Observatory, P. O. Box O, Socorro, NM 87801 USA.; The National Radio Astronomy Observatory is facility of the National Science Foundation operated under cooperative agreement by Associated Universities Inc.

²Institute for Astronomy, University of Hawaii, Honolulu, Hawaii, 96822, USA

³Canada-France-Hawaii Telescope, Kamuela, Hawaii, 96743, USA

⁴Department of Physics & Astronomy, Rutgers University, 136 Frelinghuysen Rd, Piscataway, NJ 08854, USA

Subject headings: cosmology: observations — galaxies: evolution — galaxies: starburst — galaxies: active — galaxies

1. Introduction

We are building a deep multi-wavelength picture of the sky in the SWIRE Spitzer deep field, 1046+59, which was chosen to be ideal for deep radio imaging. In paper I we discussed the 20cm continuum survey . The present 90cm survey allows us to study the radio spectra of the general source population. For Jansky and mJy sources, very steep radio spectra often are associated with very high redshifts, although the physical origin of this effect remains unclear (e.g., Miley & De Breuck 2008). A large population of very steep spectrum, μ Jy sources might suggest a corresponding high redshift μ Jy population. On the other hand, flatter radio spectra are often thought to be connected with synchrotron self-absorption or free-free absorption, although other mechanisms could potentially produce such spectra. Combined with other information the low frequency spectral energy distribution has the potential to give us unique insight on the physics of black-hole-driven AGN and star-forming galaxies. In this paper we report our 90cm observations with the VLA and some analysis of these radio data combined with our 20cm survey of the same field from paper I. In future papers in this series, we will combine these data with redshift measurements and observations at other wavelengths.

2. Observations, Reduction and Cataloging

Observations were made of a single pointing center position, $10^h46^m00^s$, $59^\circ01'00''$ (J2000), with the VLA in A and C configurations for a total of almost 85 hours on-source between February 2006 and January 2007. However, due to the ongoing EVLA upgrade, only 22 working antennas were typically available in A and 18 in C. Thus the total integration time was equivalent to ~ 63 hours in A and ~ 5 in C, with correspondingly less uv coverage. In Table 1, we summarize the parameters of the observing runs. Since the total time is dominated by the A configuration, the final image for analysis had a resolution $\sim 6''$ and FWHM FOV of 2.3° . The data were all taken in spectral-line mode 4 using on-line Hanning smoothing, resulting in fifteen 390.625 kHz channels in each of 2 IFs (centered at 321.5 and 327.5 MHz) and each of two polarizations. Five second integration times were used in the A configuration and 10 seconds in C. The integration times and channel bandwidths were chosen to minimize tangential and radial smearing of the images away from the field center. This combination of parameters produces the best compromise for imaging sensitivity and

quality possible with the current VLA correlator, which dates from the 1970's. The finite bandwidth of the spectral channels still produces some radial smearing of the image away from the field center which we take into account in the analysis of the image.

2.1. Calibration & Editing and Imaging

For calibration, editing, and imaging a procedure similar to the one described in paper I was used. The Baars flux density scale (Baars et al. 1977) was adopted using 3C286 as the flux calibrator. Two of the 15 channels in each IF were deleted due to interference which is generated by the VLA itself and which should disappear when the EVLA is completed. Unless otherwise stated, the AIPS package (Greisen 2003) was used to reduce these data.

A faceted, low resolution image (90" clean beam) with a radius of 15 degrees was made to find interfering sources far from the area of interest. Facets centered on all very bright NVSS sources (> 30 Jy) out to 100 degrees from the field center were also included in this exploratory image. From this search 288 facets, each with 500×500 pixels, were chosen to cover a central region 93' in radius and all the other bright sources found in the low resolution search. The facets were defined using the task SETFC which creates a set of overlapping circular regions within the square facets to cover the entire desired field. Then IMAGR was used to deconvolve all the facets together, using the standard Cotton-Schwab-Clark clean algorithm (Schwab 1984). The cell size for the final image is 2" and the clean beam size is $6.37'' \times 5.90''$ $pa = 86^\circ$.

Clean images from the first day of the observations were then used as fiducial models for each of the other days. Phase and amplitude calibrations were made of each of the other days using the clean components from the first day images. The A configuration data for each IF and polarization were then combined into a smaller, averaged dataset using STUFR and images for the full datasets were made. The C configuration data were also calibrated using the full A configuration images. The A and C datasets were then combined using DBCON and images were made separately for each IF and polarization.

After making these images there remained some significant residual structures in the central two degrees of the image due to bright sources located outside the central region. These residuals are likely due to 1) differences in the primary beam patterns from antenna to antenna due to the very simple dipole feeds used on the VLA and 2) the rotation with parallactic angle of the sensitivity pattern on the sky during the synthesis. For bright sources in the outskirts of the field, these variations in sensitivity produce local gain variations which are not taken into account in the imaging and self-calibration process. In order to deal with

this type of error, an AIPS procedure, PEELR, was developed and made generally available in the AIPS package. In PEELR the best clean model is subtracted from the self-calibrated uv data, except for the facet containing the bright source responsible for the residuals. These mostly residual data are then self-calibrated as a function of time using only the model for the bright source. This process allows the variations in gain due to the actual primary beam of each antenna to be tracked in time. This local complex calibration is then applied to the mostly residual data and the model for the bright source subtracted from the locally calibrated result. This operation removes, as accurately as possible, the contribution of the offending source. The inverse of the local calibration is applied to the resulting fully residual data and the full clean model added back to the uv database. If there are several offending sources, this process can be repeated for each source as it was in the present case. When the “peeled” dataset is then imaged, the effects of the offending outlying sources are significantly reduced. Techniques like this one have been used by others, but only by combining several different steps and perhaps not quite in the same way as described here.

The resulting images still showed radial smearing for bright sources in excess of what is expected from the finite bandwidths. To explore these errors we subtracted the clean component model from each visibility dataset and made spectral line image cubes from the residual visibilities. For facets containing bright sources far from the field center, these images showed frequency-dependent artifacts which are likely due to the different slopes of the bandpass across each spectral channel. This instrumental problem causes the effective observing frequency for each channel to be slightly different than is assumed and thus the uvw coordinate for each channel used in the imaging to be slightly in error. As a consequence, the source image in each channel is slightly mis-registered, producing a radial smearing for very bright sources far from the field center. To remove the error pattern due to this effect we cleaned the spectral residual image cubes in facets containing bright, outlying sources and subtracted the resulting clean components from the corresponding visibility data. This reduced the error pattern significantly.

The resulting four sets of 288 facets were then made into single images using FLATN. Finally a weighted average of the four images was made, weighting by the $1/\text{rms}^2$, as determined from the IMEAN fit to the pixel histogram. This final image still showed a weak, large-scale error pattern due to the imperfections of the corrections described above. For the final image used for most of the analysis, the AIPS program MWFLT was used to calculate the “mode” of the image over an $82'' \times 82''$ support window and the result was subtracted from the image. For sources approaching this scale size the image before MWFLT was used for analysis but for the vast majority of the sources the MWFLT image was used.

The rms noise near the center of the final image is $\sim 70\mu\text{Jy beam}^{-1}$ making it one of

the most sensitive surveys to date made at such a long wavelength. The corresponding value for the 20cm image discussed in paper I is much lower, $\sim 2.7\mu\text{Jy beam}^{-1}$. For a spectral index, $\alpha_{20}^{90} \sim 0.7$ the ratio of flux densities between 90cm and 20cm is ~ 2.8 . Thus the effective sensitivity difference in the field center is about one order of magnitude. However the resolution for the full sensitivity image is about $4\times$ worse at 90cm than at 20cm. Also the primary beam at 90cm is about $4\times$ wider. Since, many of the sources are resolved at 20cm and because most are more than a few arcminutes from the field center, the sensitivity difference is not as large as at the field center and can be better at 90cm than at 20cm very far from the field center. Thus in comparing the two surveys we need to keep in mind the local properties of each source in the image of interest at each wavelength.

2.2. Cataloging

Although the primary beam has a diameter of 2.3° and the region we imaged extends out far beyond this limit, we chose to catalog the region within 1° of the field center. This two-degree diameter field-of-view covers more than the entire field we are studying at other wavelengths. Moreover, the primary beam shape becomes less well known beyond one degree and the smearing due to the finite channel width begins to become important beyond this radius. As with the 20cm survey we include the radial smearing due to the finite bandwidth in our Gaussian fits. In the present case the angular FWHM of the radial smearing function is approximately $0.0012\times$ (the distance from the field center). In the worst case, for a point source at the maximum cataloged radius from the field center, this bandwidth smearing amounts to a decrease in the peak brightness at full resolution of $\sim 18\%$. As for the 20cm survey, we convolved our $\sim 6''$ images to resolutions of $12''$ and $24''$ to increase the detection sensitivity for large sources. This exercise was much less important than it was for the 20cm survey, but it did yield higher S/N detections for a subset of the survey.

As for the 20cm survey, the AIPS program SAD was used for forming the initial source lists. A catalog for each resolution was formed down to a peak signal/noise (S/N) of 4.5. The residual images from SAD were then searched to find any remaining sources missed by the program with a S/N greater than 5.0. For sources with a S/N close to 5.0, the fitting process was repeated by hand with JMFIT, using the local rms estimate over a region 100 pixels in diameter. In this way a reliable list of sources with S/N of 5.0 or greater at each resolution was compiled. For both SAD and JMFIT, the smearing due to the finite bandwidth was included in the fitting process. As described for the 20cm survey in paper I, the best description of each of the sources with a peak $S/N \geq 5$ at one of the resolutions analyzed was included in the final 90cm catalog. In order to allow for a variety of potential

calibration errors, a 3% error term proportional to the total measured flux density of each source was folded into the errors in quadrature, as was done for the 20cm survey.

3. Results

3.1. Radio Catalog

In Table 2, we give the first ten lines of the radio catalog; the full table is provided electronically. Column (1) contains the source number. If the source has a number less than 3000, then it was found with a $S/N \geq 5.0$ from running SAD on the full resolution image. Sources with numbers ≥ 10000 were found in lower resolution images or in checks of the residual images. Numbers beginning with 12 were measured on a $12''$ resolution image. If the number begins with 24 then we used a $24''$ resolution image. The lower resolution fits were used in the table when they indicated a significantly larger total flux density for the source in question. Each of these cases was also investigated by eye to confirm the result. Columns (2) and (3) contain the radio RA and Dec along with the estimated error. Column (4) contains the corrected peak flux density from the map in μJy per beam. In column (5) we list the corrected total flux density. In column (6) we give the estimated error in the total flux density. Column (7) contains the peak S/N. The error for column (4) can be recovered by dividing column (4) by column (7). We give the S/N as opposed to the error since the S/N was used to define the catalog cutoff and later is used in the calculation of $\log N - \log S$. In column (8), we give the best fit deconvolved size in arcseconds. If a resolved two dimensional Gaussian was the best fit, we give the major and minor axis size (FWHM) and the position angle. Upper limits are given for sources which were unresolved based on the results of JMFIT or SAD. When the minor axis is unresolved, we give “0” as the minor axis size in the table and assume a one-dimensional Gaussian size when estimating the total flux density. sources with very large sizes, for which only a largest angular size is given in column (8), sizes and total flux densities were estimated directly from the images using the AIPS routines, IMVAL and TVSTAT.

3.2. Angular size distribution

The 90cm catalog covers a larger area than the 20cm survey but at a significantly lower sensitivity. This means that the 90cm survey samples sources in a higher range in 20cm flux density with different properties in angular size and absolute radio luminosity than our 20cm survey. In Figure 1 we show the median angular size – 90cm flux density distribution. Above

3 mJy we resolve most of the sources but below 3mJy most of the sources are relatively small. Our 20cm results for the same sources reported in paper I show that the typical median size is $\sim 1.2''$. This trend in the measured median sizes at 90cm is shown in Table 3 and Figure 2. Although similar resolution data have not been reported at 90cm these results are also consistent with previous results at higher frequencies, extrapolated to 90cm (Windhorst 2003).

Some of the 90cm sources have larger sizes than the corresponding 20cm counterparts. For these sources we checked the flux densities and sizes at 20cm by smoothing to the resolution of the 90cm detection images. For most of these sources the lower resolution 20cm sizes and flux densities agree well with the fits at the original resolution. The total flux density changed by more than 10% for only three individually cataloged 20cm sources (00061, 01186 and 01193). In making the 20cm catalog, the larger flux densities at lower resolution were rejected because the S/N was significantly higher on higher resolution images which fitted smaller sizes. The 90cm survey is also more sensitive to smaller spatial frequencies and any steeper spectrum, more extended emission. While these results do not change any of the conclusions in paper I, we are likely a little incomplete for the largest sources at 20cm, especially near the bottom of the catalog. For the spectral index analysis below we have used the 20cm fits from imaging at 90cm resolution.

3.3. Spectral Indices

3.3.1. 90cm selected sources

For our spectral index analysis we restrict ourselves to sources within $20'$ of the field center. At that radius we are complete at 20cm and beyond that distance from the field center the uncertainty due to the primary beam correction at 20cm becomes significant. Since the 20cm image is so deep, almost all the 90cm sources within $20'$ of the field center have counterparts which we can use to determine spectral indices. Two 90cm sources (01492 and 01501) were detected on the 20cm $6''$ resolution image only with $S/N < 5$. Three more sources (00766 $\alpha > 1.46$, 01346 $\alpha > 1.71$ and 01491 $\alpha > 1.84$) have no 20cm counterpart with a $S/N > 3$. However, these three sources all have low 90cm S/N detections, $5.0 < S/N < 5.6$, and have no counterparts on our deep optical/NIR images (Strazzullo et al. 2009) or our deep 50cm GMRT image (Owen et al. 2009). These sources either have very steep spectra and are very distant or they are spurious. We choose to leave them out of the following discussion but note that there may be a small, very steep spectrum tail to the distribution.

In most other cases, the positions and sizes of individual sources in 20cm and 90cm

catalogs agree well with one another and the spectral index is calculated from the values listed in the respective tables. In cases where the cataloged 20cm and 90cm parameters do not agree well in size and/or position the sources were investigated on the respective 20cm and 90cm images by eye. When more than one 20cm source corresponds to a 90cm source the flux densities of the 20cm sources were summed. If only the 90cm source is apparently resolved but the 20cm source size implies that the 90cm source should be unresolved, then the peak flux on the highest resolution 90cm image and the total 20cm flux density were used to calculate the spectral index (e.g. 90cm source 00727). If both the 20cm and 90cm source are resolved then the peak flux density at both 20cm and 90cm is used from images at the resolution of the cataloged 90cm source (e.g. 90cm source 12407). In Table 4 we give the first ten lines of the electronic table summarizing the 90cm-selected spectral indices, including 90cm source 00727 and 12407 discussed above. If we needed to sum more than one 20cm flux density, then we give the total in column 5. Otherwise we give the cataloged total flux densities but indicate with a note the few cases where discrepant size estimates drive us to use peak flux densities for the corresponding spectral index estimate.

Figure 3 contains the observed histogram of 90 to 20cm spectral indices ($S \propto \nu^{-\alpha}$) for sources detected above 5 sigma at 90cm. In Table 5 we summarize the statistics for these sources as a function of 90cm flux density and size. The mean and median spectral indices are ~ 0.7 for all of our subsets. This value is flatter than the mean 408-1407 MHz spectral index of 0.92 from 5C12 for sources detected at 408 MHz above 40 mJy (Benn et al. 1982). We have only a few sources with 90cm flux densities > 40 mJy in our 90cm survey, so our results are consistent with a flattening in the mean spectral index below the 5C12 characteristic flux density. The deeper LBDS 327 MHz survey has a 90cm-selected, 327-1462 MHz median spectral index shifting from ~ 0.9 above 100 mJy, to ~ 0.7 between 10 and 100 mJy, and then down to ~ 0.5 between 3.6 and 10 mJy (Oort et al. 1988). We agree with their estimate in the 10 – 100 mJy range but do not find the flatter median spectral index below 10 mJy near the bottom of the LBDS survey.

3.3.2. 20cm selected sources

Most recent work on deep fields involves surveys at 20cm, so it is also interesting to study the spectral index distribution when selecting the sources at 20cm. Since most of the 20cm sources are not detected directly at 90cm, we must use a combination of a high 20cm flux density cutoff to study the stronger 20cm sources individually and stacking subsets at 90cm in order to study the fainter 20cm population. Most of the weaker sources are much smaller than the size of the synthesized beam of our 90cm survey (see paper I). Those sources

that are expected to be unresolved at 90cm are suitable for stacking analysis.

For the high flux density subset, we select only 20cm sources with total flux densities $> 100\mu\text{Jy}$ from paper I within $20'$ of the field center. In Table 6 we show the first 10 lines of the electronic table of the 90cm–20cm spectral indices for these sources. In Figure 4 we plot the histogram of the spectral indices of these sources against their 20cm flux densities. Since, in this subset of sources, many of the sources are not detected above 3 sigma at 90cm, we plot the blue area for sources detected above 3 sigma while the red area represents the 3 sigma upper limit corrected for the observed 20cm source size. The median spectral index is $0.52(0.04)$ including the upper limits, significantly flatter than the 90cm selected sample and samples with brighter limiting flux densities selected at 20cm. In Figure 5 we show spectral index plotted against the 20cm flux density for sources with $S_{20} > 100\mu\text{Jy}$. This plot shows the sources with 90cm upper limits as red circles clearly delineating the section of the plot which is not allowed due to the 90cm sensitivity. Even with this high limit on the 20cm catalog, 37% of the sources with $100\mu\text{Jy} < S_{20} < 1000\mu\text{Jy}$ have upper limits at 90cm; thus we cannot determine the details of the dependence of the spectral index distribution on 20cm flux density for $S_{20} < 1\text{ mJy}$ from the properties of individual sources.

In order to study the spectral index distribution down to the bottom of the 20cm catalog, we need to use stacking on the 90cm image. Since we need to restrict the stacks to angular sizes which are effectively unresolved, we omit a modest, but significant number of sources that are resolved by the 90cm synthesized beam. In the following discussion, we divide the sources into subsets by ranges of 20cm flux density and also split the subsets into sources which are $> 3''$ and $\leq 3''$. In Paper I we found that sources with $S_{20} < 1\text{ mJy}$ have a median size of $\sim 1''$, unlike the stronger sources individually detected at 90cm. If we omit from the stacking analysis the $\sim 10\%$ of sources with $S_{20} < 1\text{ mJy}$ that have sizes $> 3''$, we expect that the spectral properties of the $\leq 3''$ subsets should be close to those of the full population. In stacking each subsample with flux densities at 20cm $< 1\text{mJy}$, we extract the observed 90cm brightness in $\mu\text{Jy}/\text{beam}$ at the position of the 20cm source. For small sources this should be a good estimate of the total flux density in μJy . Within the subset, we then calculate the mean and median flux densities at both frequencies. The spectral index computed from the two mean flux densities and that computed from the two median flux densities are listed for each subset in the bottom six lines of Table 7. The errors in Table 7 are calculated assuming counting statistics from the total number in each subset, combined in quadrature with an assumed standard deviation for the population of spectral indices of 0.30 which seems appropriate based on the higher flux density, 90cm-selected, spectral indices but is only an educated guess.

For sources stronger than 1 mJy at 20cm, all except one have a detection at 90cm.

Excluding this source we can calculate the median and mean spectral index for subsets selected by source flux density and size and these are listed in Table 7. In Figure 6 we summarize the results graphically. Above 1 mJy, where we can study both size subsets, the more resolved sources have steeper spectra than the $\leq 3''$ subset. The mean and median spectral indices continue to flatten for the full population. For the small sources, the median and mean spectral indices flatten to $\sim 0.3 - 0.5$. Below 1 mJy the small source medians and means continue to be in the range $\sim 0.3 - 0.5$, but with a clear trend to steeper spectra at the lowest flux densities in the 20cm sample.

3.3.3. 90cm versus 20cm selection

The results for the spectral indices are quite different depending on whether we select the samples at 90cm or 20cm. At 90cm we find very constant mean and median spectral index of ~ 0.7 down to the survey limit of $300\mu\text{Jy}$. No obvious dependence is found on angular size. Approximately the same result is found in the 90cm selected sample down to 1 mJy at 20cm which would correspond to ~ 3 mJy at 90cm with a spectral index ~ 0.7 . However, sources $> 3''$ in size tend to have steeper spectra than those $\leq 3''$. Below 1 mJy at 20cm, many more sources do not have detections than would be expected if the ~ 0.7 spectral index continued. For these and weaker sources, we are forced to consider only small sources since the surface brightness sensitivity at 90cm is not high enough to detect sources of all angular sizes. For this population of small sources, we find much flatter median and mean spectral indices, $\sim 0.3 - 0.5$. This result suggests that there is a smaller size, 20cm source population which is attenuated enough at 90cm, relative to an $\alpha_{20}^{90} \sim 0.7$, to affect the median source properties relative to a 90cm-selected population.

3.4. Log N - Log S

The calculation of the 90cm log N - log S is much easier than for 20cm in paper I because 1) we only consider a radius of one degree which doesn't reach the half power point of the primary beam and 2) the synthesized beam is bigger, $\sim 6.2''$ so fewer sources are resolved, and 3) the fractional channel bandwidth is smaller. These parameters dramatically reduce the problems we faced in paper I and allow us to perform a simpler analysis. Only below 1 mJy is the incompleteness due to source size an issue. For weak sources we use the same formalism as in paper I to account for missing sources due to resolution and bandwidth smearing and the same assumed source size distribution. Even for the weaker sources, since the resolution is lower, the impact of these corrections is very small. In Table 8,

we summarize our results for the 5 sigma catalog only, unlike paper I where we performed a more complicated calculation with a variable S/N cutoff.

In Figure 7, we plot our results along with the 327 MHz results for LBDS (Oort et al. 1988) for their 5 sigma catalog and the 5C12 results from 408 MHz scaled by their quoted mean spectral index of 0.9 to 324.5 MHz (Benn et al. 1982). The results are in general agreement and our additions show that we have reached the flat region of the counts seen at other frequencies near 3 mJy. This change in slope also corresponds roughly to the minimum in the spectral index distribution seen in Figure 6.

4. Discussion

These data fill out the picture of the meter-wavelength radio sky a bit more clearly, building on the earlier work cited above, but also raise new questions. Instead of finding a large steep spectrum population, we find flatter spectra for the subset of sources with angular sizes $< 3''$ and $S_{20} < 10\text{mJy}$. We also find that the differential log N - Log S at 90cm flattens in roughly the same flux density range ($S_{90} < 5\text{ mJy}$). Thus the nature of the meter wavelength population seems to be changing in the few mJy range. Often a trend toward flattening radio spectra at higher frequencies and the corresponding change in slope of log N - log S is attributed to star-forming galaxies becoming dominant (e.g., Windhorst 2003). However, only for 20cm luminosities $< 10^{23}\text{ W Hz}^{-1}$ are star-forming galaxies more common than AGN (e.g., Condon et al. 2002). For sources with $S_{20} > 1\text{mJy}$ (equivalent to $S_{90} > 2\text{mJy}$ with $\alpha_{20}^{90} \sim 0.5$) to have a 20cm luminosity $< 10^{23}\text{ W Hz}^{-1}$, their redshift would have to be < 0.2 . This redshift is much too low for most such mJy sources to be dominated by star-formation, since we find a median $z \sim 1$ for our sample (Strazzullo et al. 2009). Thus it seems likely that the changes we are observing are in the AGN population. Furthermore, spectral studies at wavelengths $< 20\text{cm}$, show that the typical μJy source has a quite steep spectrum, $\sim 0.8 - 0.9$ (Fomalont et al. 2006). Therefore our 20cm-selected μJy sources with flatter spectra cannot be due to free-free emission, since the flat spectrum free-free emission should be less important at longer wavelengths.

One might think that flatter spectra in AGN might be due to synchrotron self-absorption as is seen in many beamed radio galaxies and quasars. However, our work in paper I and other studies (e.g., Muxlow et al. 2005; Fomalont et al. 2006) show that the typical sizes for these sources are $\sim 1''$. This argues against synchrotron self-absorption being dominant since that mechanism requires sizes $\ll 1$ milliarcsecond to be important. One possibility is that the flatter spectra could result from the combination of a relatively flat-spectrum AGN jet with a spectral index ~ 0.5 (e.g., Bridle & Perley 1984; Butcher et al. 1980) and a

synchrotron self-absorbed core.

Since the sources are relatively small, free-free absorption is a possibility. Free-free absorption for such sources depends in general on the details of the clumpiness of the absorbing thermal gas and its geometric relation to the synchrotron emitting medium. In star-forming systems which have been well studied, the radio emission is extended more uniformly throughout the galaxy than the dust or the HII regions (Hoernes et al. 1998; Murphy et al. 2008). Free-free absorption is also seen on small scales in some radio AGN (e.g., Walker et al. 1994; Gallimore et al. 2004). For a uniform density foreground medium with a temperature $\sim 10^4\text{K}$, the characteristic free-free absorption turnover frequency is $\nu_t(\text{MHz}) \sim 0.5n(\text{cm}^{-3})l^{0.5}(\text{pc})$, where l is the projected pathlength. For example, for a typical source in our sample with a size of $1''$ at $z \sim 1$, a typical radius is ~ 4 kpc and, for a rest frame turnover frequency of ~ 300 MHz, one needs a density of 10 cm^{-3} , which would correspond to a mass of $\sim 6 \times 10^{10} M_\odot$ if uniformly distributed in a sphere. A more realistic model with a smaller filling factor and a different geometry reduces the mass estimates but if free-free absorption is important then a reasonably large mass of ionized gas must be involved. The flattening could also be due to ionization losses as has been suggested for some star-forming galaxies (e.g., Thompson et al. 2006). In any case, the flatter spectra and the flatter counts observed below 3 mJy suggest a change in the nature of the population below this flux density level which is not well understood. We will discuss this point further in future papers where we add redshifts and data from other wavelengths to the analysis.

5. Conclusion

We have presented a very sensitive 90cm image of the SWIRE deep field. This image combined with our uniquely sensitive 20cm image of this field allows us to study the meter wavelength spectral indices as a function of flux density for the μJy radio population. For 90cm-selected sources the properties of the sources are consistent with previous work with a mean spectral index near 0.7 and few very steep spectrum sources. Thus no large population of very steep spectrum μJy sources seems to exist down to our limiting flux density.

For the subset of sources selected at 20cm with sizes $< 3''$ (which contains about $\sim 90\%$ of all 20cm-selected sources < 1 mJy), the mean and median spectral indices flatten from $\alpha \sim 0.7$ to $\alpha \sim 0.3 - 0.5$ below 10 mJy with a trend toward steeper spectra at the lowest flux densities. The 90cm log N-log S counts flatten below 5 mJy as they do at corresponding low flux densities at higher frequencies. The change in the source properties at a few mJy is not well understood but probably involves the AGN population, not primarily star-formation-dominated galaxies.

REFERENCES

- Baars, J. W. M., Genzel, R., Pauliny-Toth, I. I. K., & Witzel, A. 1977, *A&A*, 61, 99.
- Benn, C. R., Grueff, G., Vigotti, M. & Wall, J. V. 1982, *MNRAS*, 200, 747.
- Bridle, A. H., & Perley, R. A. *ARA&A*, 22, 319.
- Butcher, H. R., van Breugel, W. & Miley, G. K. 1980, *ApJ*, 235, 749.
- Condon, J. J., Cotton, W. D, & Broderick, J. J. 2002, *AJ*, 124, 675.
- Fomalont, E. B., Kellermann, K. I., Cowie, L. L., Capak, P., Barger, A. J., Partridge, R. B., Windhorst, R. A. & Richards, E. A. 2006, *ApJS*, 167, 103.
- Gallimore, J. F., Baum, S. A. & O’Dea, C. P. 2004, *ApJ*, 613, 794.
- Greisen, E. W. 2003, in *Information Handling in Astronomy – Historical Vistas* (ed. A. Heck), Kluwer, Dordrecht, 109.
- Hoernes, P. Berkhuijsen, E.M., & Xu, C. 1998, *A&A*, 34, 57.
- Miley, G. & De Breuck, C. 2008, *A&A Rev.*, 15, 67.
- Murphy, E. J., Helou, G., Kenney, J. D. P., Armus, L., & Braun, R. 2008, *ApJ*, 678, 828.
- Muxlow, T. W. B., Richards, A. M. S., Garrington, S. T., Wilkinson, P. N., Anderson, B., Richards, E. A., Axon, D. J., Fomalont, E. B., Kellermann, K. I., Partridge, R. B., & Windhorst, R. A, 2005, *MNRAS*, 358, 1159.
- Oort, M J. A., Steemers, W. J. G. & Windhorst, R. A. 1988, *A&AS*, 73, 103.
- Owen, F. N. & Morrison, G. E. 2008 *AJ*, 136, 1889 (paper I).
- Owen, F. N. et al. 2009 (in preparation).
- Schwab, F. R. 1984, *AJ*, 89, 1076.
- Thompson, T. A., Quataert, E., Waxman, E., Murray, N., & Martin, C. L. 2006, *ApJ*, 645, 186.
- Strazzullo, V. et al 2009 (in preparation).
- Walker, R. C., Romney, J. D. & Benson, J. M. 1994, *ApJ*, 430, L45.
- Windhorst, R. A. 2003, *New A Rev.*, 47, 357.

Table 1. Observing Runs Summary

Configuration	Start date	End date	Hours
A	06Feb19	06May17	77.1
C	07Jan04	07Jan05	7.9

Table 2. Radio Source Catalog

Name	RA(2000.0)	Dec(2000.0)	Peak $\mu\text{Jy}/\text{b}$	Total μJy	Error μJy	S/N	Size " x" pa= $^{\circ}$
00018	10 38 14.59(0.03)	59 02 36.0(0.1)	2778	5425	320	26.7	12x2pa= 91
12017	10 38 24.64(0.10)	59 00 35.1(0.6)	1423	2498	340	10.9	15x6pa=64
00036	10 38 25.64(0.11)	59 05 58.0(0.5)	620	892	241	5.5	8x0pa=113
00043	10 38 29.75(0.03)	58 52 05.0(0.2)	1071	1071	115	9.7	<3
12045	10 38 31.50(0.03)	58 47 09.0(0.4)	3024	4763	348	22.2	14x3pa=13
00051	10 38 34.56(0.07)	59 15 15.3(0.5)	629	629	116	5.5	<6
00058	10 38 37.82(0.01)	59 09 45.2(0.1)	5423	5423	196	49.8	<2
00059	10 38 39.16(0.01)	58 59 12.3(0.1)	28469	28570	874	271.1	<2
00065	10 38 42.27(0.05)	59 01 10.5(0.3)	919	919	118	8.0	<4
00068	10 38 43.23(0.07)	58 43 14.2(0.6)	594	594	117	5.1	<4

Table 3. 90cm Source Size Statistics

$\log(S_{90})^a$	Num ^b	Size ^c "	$\log(S_{90}^d)$
5.0 – 6.1	20	17.0(7.9)	5.25
4.0 – 5.0	95	7.0(4.5)	4.41
3.5 – 4.0	126	4.5(2.7)	3.71
3.0 – 3.5	335	< 4	3.18
2.5 – 3.0	859	< 5	2.76

^aRange of the log of 90cm flux densities with S_{90} in μJy

^bNumber of sources in interval

^cMedian size with error in median in parenthesis

^dMedian of the 90cm flux density of the subsample in μJy

Table 4. Spectral Indices for 90cm Selected Sources

Name 90cm	α_{20}^{90a}	Error α_{20}^{90}	S_{90} μJy	S_{20} μJy	Res ^b 90cm	Size "	Res ^b 20cm	Size "	Note ^c
00725	0.57	0.07	758	330.2	<	4	r	2.6	
00727	0.48	0.11	813	211.4	r	7	<	2.4	*
00728	-0.40	0.04	1616	2906.2	<	3	r	1.5	
00733	0.29	0.04	1219	803.6	<	1	r	0.8	
00737	0.48	0.04	3000	1487.5	r	2	r	2.0	
12407	0.90	0.06	1211	272.4	r	12	r	7.0	*
00744	0.72	0.12	390	136.3	<	6	r	2.8	
00755	0.46	0.06	2090	1069.1	r	9	r	8.3	
00756	0.86	0.12	402	114.4	<	5	<	2.4	
00761	0.33	0.09	512	314.3	<	3	r	1.3	

^a90cm-20cm spectral index, $S \propto \nu^{-\alpha}$

^b'<': next column upper limit, 'r': next column deconvolved major axis

^c*: Spectral index determined from peak of equal resolution images at 20cm and 90cm

Table 5. Spectral Index Summary for 90cm Selected Sources

$\log(S_{90})^a$	Num ^b	α^c mean	α^c med	std ^d dev	$\log(S_{90}^e)$ mean ^f	$\log(S_{90}^e)$ med ^f
All						
2.5 – 5.0	229	0.68(0.02)	0.70(0.03)	0.31	3.38	2.77
4.0 – 5.0	11	0.70(0.05)	0.66(0.07)	0.17	4.48	4.37
3.0 – 4.0	56	0.68(0.04)	0.76(0.06)	0.34	3.37	3.23
2.5 – 3.0	162	0.68(0.02)	0.70(0.03)	0.30	2.72	2.67
> 3''						
2.5 – 5.0	55	0.71(0.03)	0.72(0.04)	0.21	3.68	3.02
4.0 – 5.0	7	0.75(0.08)	0.77(0.10)	0.19	4.43	4.24
3.0 – 4.0	22	0.74(0.05)	0.76(0.07)	0.24	3.40	3.25
2.5 – 3.0	26	0.68(0.04)	0.67(0.05)	0.19	2.77	2.76
≤ 3''						
2.5 – 5.0	174	0.67(0.03)	0.70(0.03)	0.34	3.22	2.70
4.0 – 5.0	4	0.60(0.04)	0.61(0.05)	0.06	4.54	4.49
3.0 – 4.0	34	0.65(0.07)	0.67(0.08)	0.38	3.37	3.23
2.5 – 3.0	136	0.68(0.03)	0.71(0.04)	0.19	2.77	2.77

^aRange of the log of 90cm flux densities with S_{90} in μJy

^bNumber of Sources in the interval.

^cSpectral Index between 90cm and 20cm defined as $S \propto \nu^{-\alpha}$.

^dEstimated standard deviation in the population

^e μJy

^fThe log of the mean or median of each subsample is given in this column.

Table 6. Spectral Indices for 20cm Selected Sources

Name 20cm	α_{20}^{90a}	Error α_{20}^{90}
00013	0.57	0.07
00016	-0.40	0.04
00021	1.02	0.06
00024	0.58	0.18
00028	0.86	0.12
00029	0.33	0.09
00030	0.82	0.10
00033	<0.28	
00037	<-0.12	
00044	-0.64	0.10

^a90cm-20cm spectral
index, $S \propto \nu^{-\alpha}$

Table 7. 20cm Selected Spectral Index Summary

$\log(S_{20})^a$	Num ^b	α^c mean	α^c med	$\log(S_{20}^d)$ mean ^e	$\log(S_{20}^d)$ med ^e
All					
2.5 – 3.0	43		0.54(0.06)		
3.0 – 5.0	24	0.58(0.09)	0.66(0.11)	3.73	3.40
4.0 – 5.0	5	0.75(0.15)	0.66(0.19)	4.21	4.16
3.0 – 4.0	19	0.54(0.11)	0.66(0.27)	4.22	4.15
> 3''					
3.0 – 5.0	12	0.75(0.10)	0.76(0.12)	3.71	3.57
4.0 – 5.0	2	0.93(0.30)	0.93(0.36)	4.19	4.19
3.0 – 4.0	10	0.71(0.11)	0.74(0.14)	3.49	3.44
≤ 3''					
3.0 – 5.0	12	0.42(0.14)	0.60(0.17)	3.75	3.35
4.0 – 5.0	3	0.62(0.15)	0.57(0.19)	4.19	4.16
3.0 – 4.0	9	0.35(0.18)	0.59(0.22)	3.28	3.29
2.5 – 3.0	28	0.47(0.07)	0.30(0.09)	2.69	2.70
2.3 – 2.5	35	0.38(0.06)	0.37(0.08)	2.41	2.41
2.1 – 2.3	87	0.49(0.05)	0.45(0.06)	2.20	2.20
1.9 – 2.1	180	0.48(0.04)	0.50(0.05)	2.00	2.00
1.6 – 1.9	485	0.50(0.04)	0.52(0.05)	1.74	1.74
1.0 – 1.6	479	0.59(0.04)	0.52(0.05)	1.46	1.46

^aRange of the log of 20cm flux densities in the interval with S_{20} in μJy

^bNumber of Sources in the interval

^cSpectral Index between 90cm and 20cm defined as $S \propto \nu^{-\alpha}$

^d μJy

^eThe log of the mean or median of each subsample is given in this column.

Table 8. 90cm differential normalized source counts for 1046+59. The table contains 1) S_l (the lower flux density limit of the bin), 2) S_h (the upper flux density limit if the bin), 3) the normalization factor and its error.

S_l	S_h	$S^{2.5}dN/dS$
μJy	μJy	$\text{Jy}^{1.5}\text{sr}^{-1}$
375	475	25.4 ± 3.7
475	600	25.9 ± 3.7
600	900	16.9 ± 1.8
900	1350	17.2 ± 2.4
1350	2000	19.3 ± 2.0
2000	3000	27.3 ± 2.9
3000	4500	30.8 ± 4.2
4500	6750	58.0 ± 7.9
6750	10000	48.7 ± 9.4
10000	20000	89.0 ± 14.7
20000	40000	243.6 ± 43.7
40000	80000	495.6 ± 105.1
80000	160000	398.1 ± 162.5

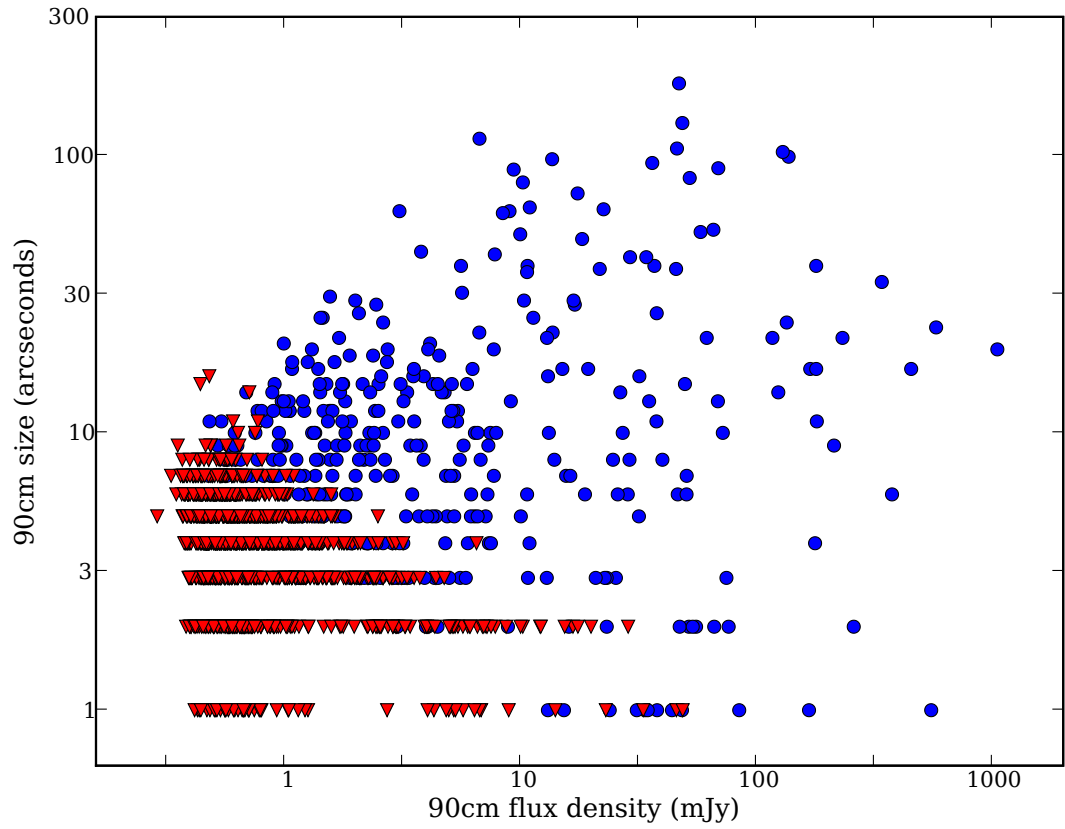


Fig. 1.— Log-Log plot of angular size versus 90cm flux density using the data in Table 2. Blue dots are for significantly resolved sources while the red triangles represent sources with upper limits to the angular size.

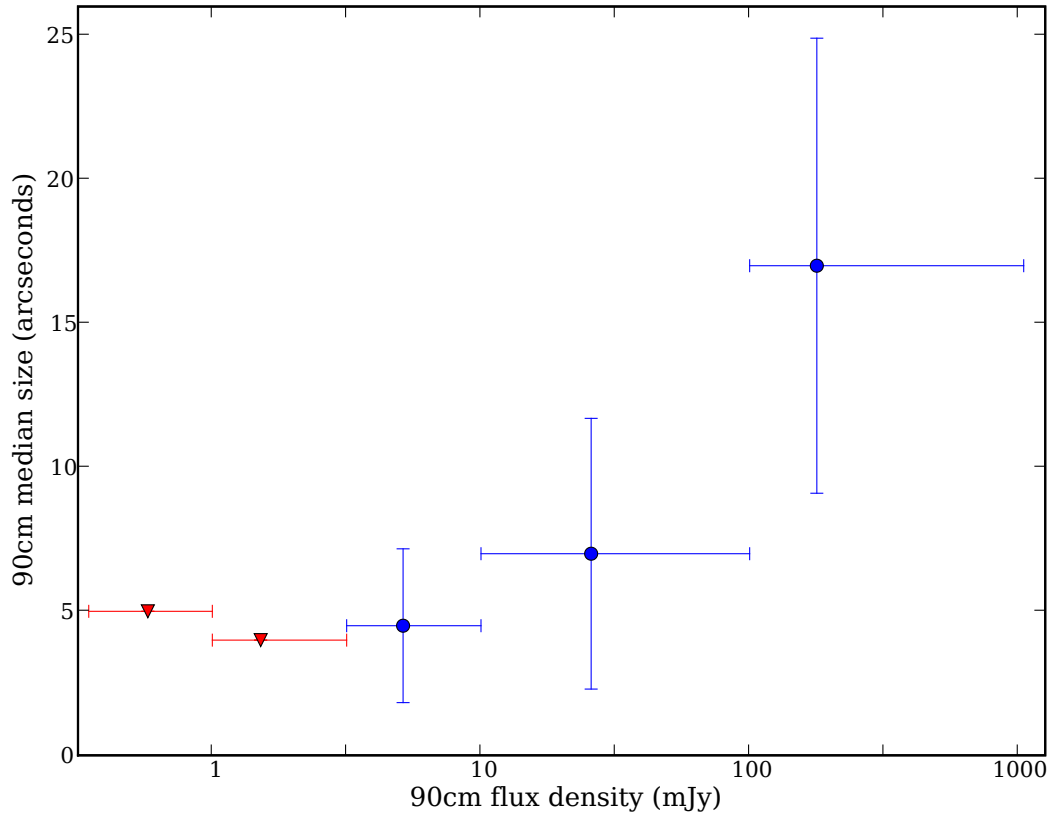


Fig. 2.— Observed median angular size for various different logarithmic ranges in 90cm flux density. Blue dots show significant detections of the median while the red triangles are upper limits to the median. The error bars in the flux densities show the size of the bins used to calculate the statistics, while the error bars in the sizes are estimated errors in the median values.

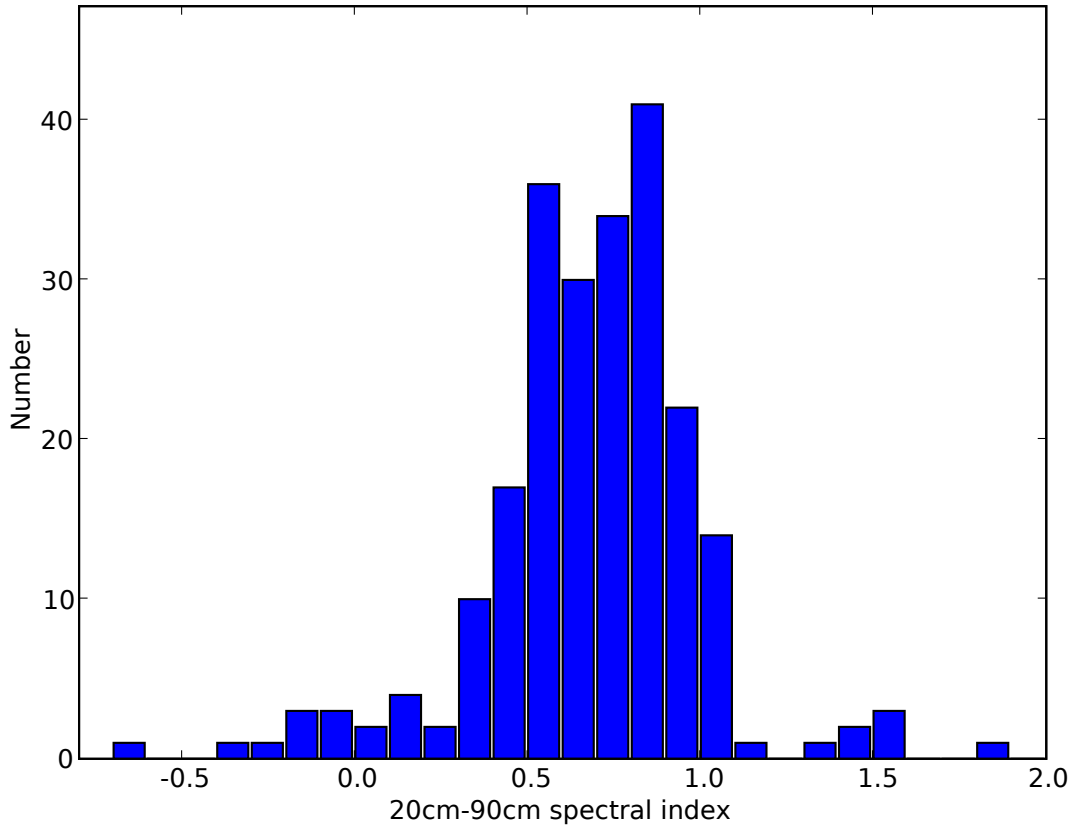


Fig. 3.— Histogram of 90cm to 20cm spectral indices for sources detected above 5 sigma at 90cm in the region cataloged for the 20cm survey.

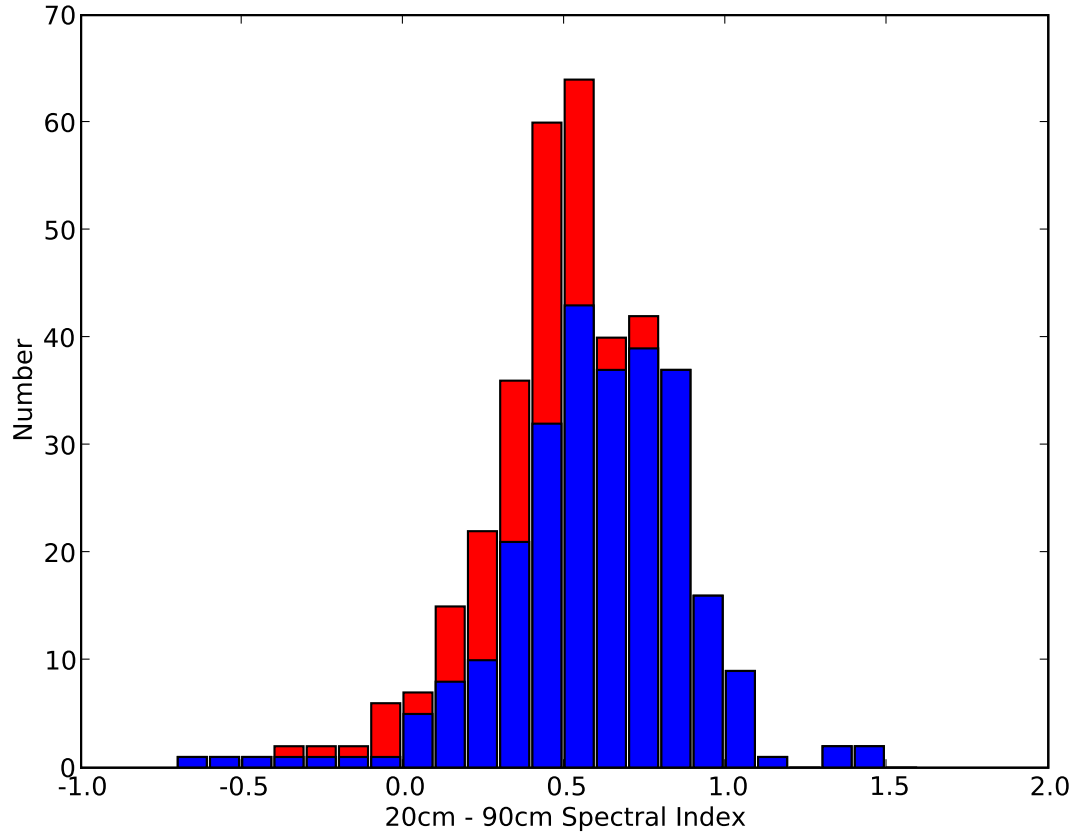


Fig. 4.— Histogram of 90cm to 20cm spectral indices for sources with 20cm flux densities $> 100\mu\text{Jy}$. Blue: measured spectral indices for 90cm sources with $S/N > 3$, Red: 3 sigma upper limits for 90cm sources with $S/N < 3$.

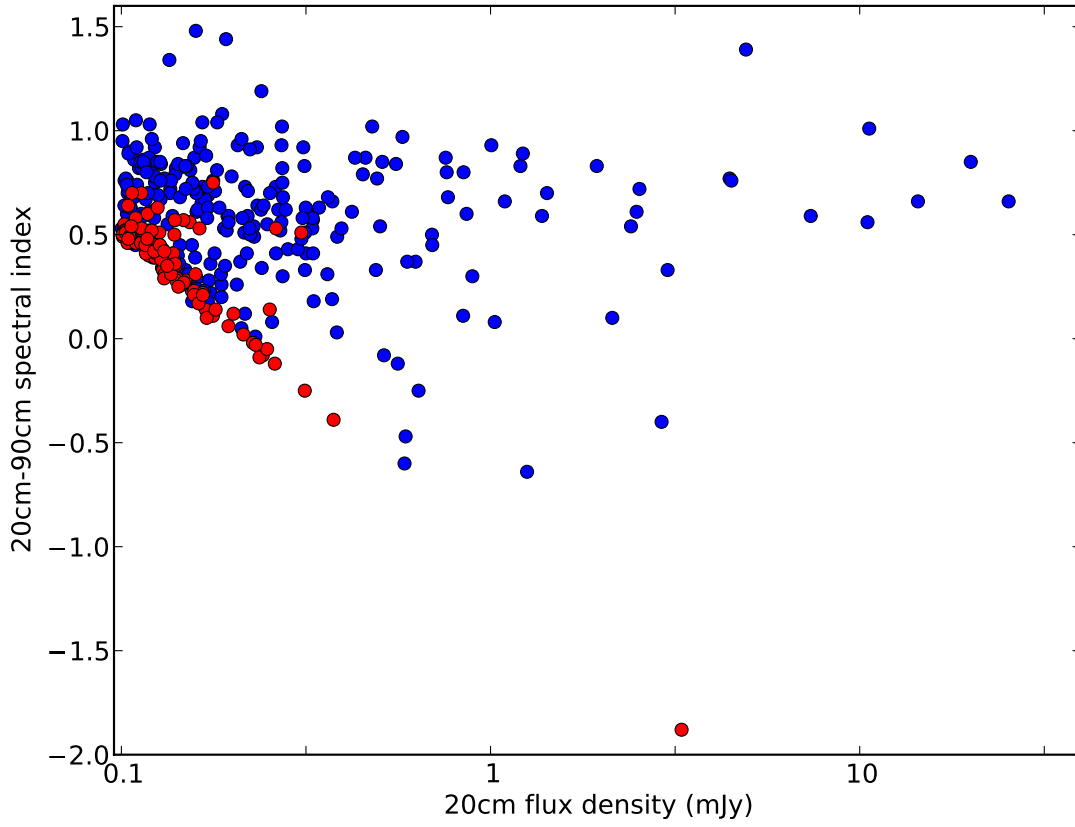


Fig. 5.— 90cm to 20cm spectral indices versus 20cm flux density plotted on a logarithmic scale. Blue dots are sources with 90cm detections > 3 sigma. Red dots are sources with 3 sigma 90cm upper limits.

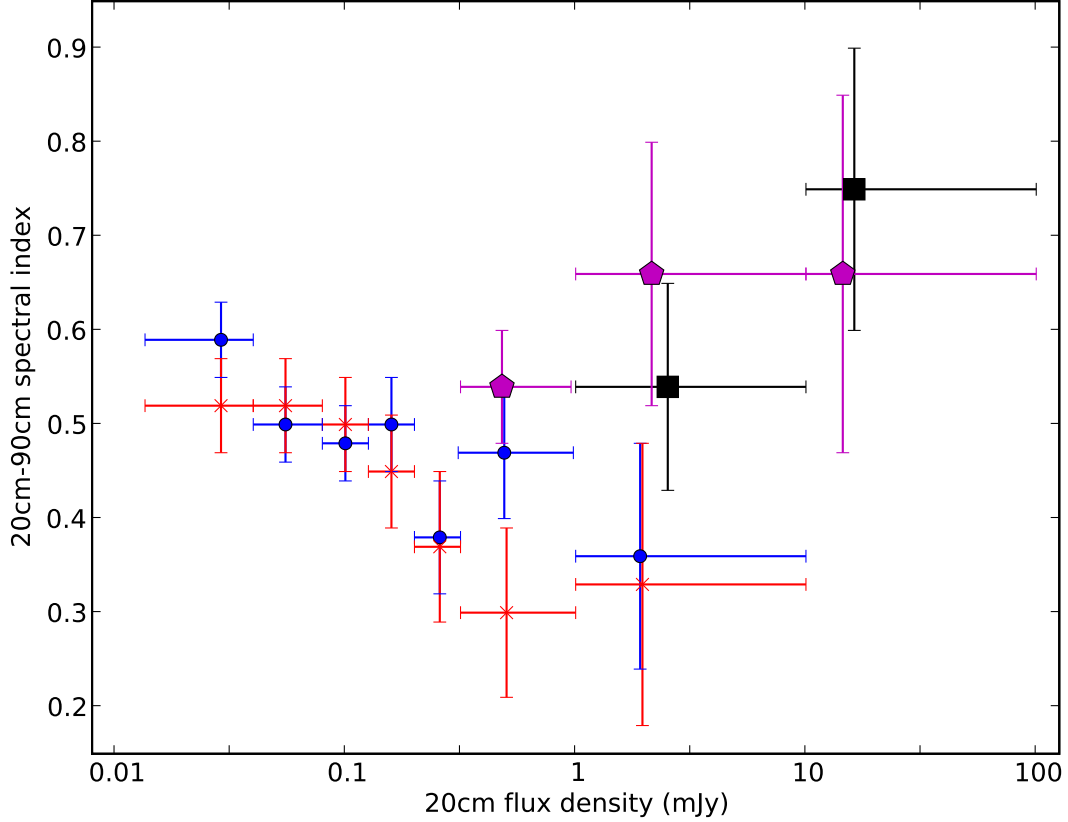


Fig. 6.— 20cm selected spectral index versus 20cm flux density in mJy in various intervals in 20cm flux density: The results are from table 7. The black squares and the magenta pentagons are the means and medians respectively for the entire sample. The blue circles and red crosses are the means and medians respectively for sources with 20cm sizes $\leq 3''$ using stacking of 90cm cutouts as described in the text. The flux density error bars show the sizes of the bins while the spectral index error bars show the estimated error in mean or median.

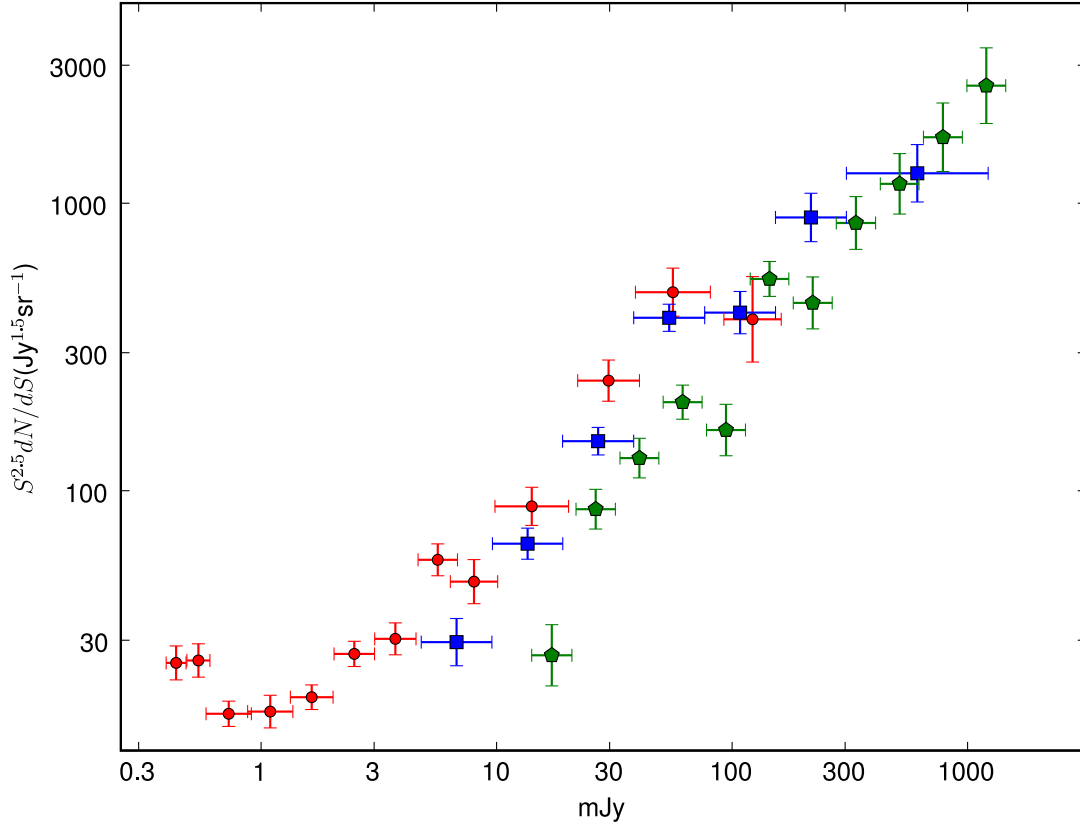


Fig. 7.— 90cm log N – log S differential distribution. Green pentagons are from the 5C12 survey at 408 MHz scaled to 324.5 MHz using a mean spectral index of 0.9 (Benn et al. 1982). Blue squares are from 327 MHz observations with Westerbork of the LBDS (Oort et al. 1988). Red circles are from table 8 in this paper.

The Deep SWIRE Field

II. 90cm Continuum Observations and 20cm–90cm Spectra

Frazer N. Owen,¹ G. E. Morrison,^{2,3} Matthew D. Klimek,^{1,4} & Eric W. Greisen,¹

ABSTRACT

We present the deepest radio continuum survey to date at a wavelength $\gtrsim 1$ meter. The observations were taken with the VLA at 324.5 MHz covering a region of the SWIRE Spitzer Legacy survey, centered at $10^h46^m00^s$, $59^\circ01'00''$ (J2000). The data reduction and analysis are described and an electronic catalog of the sources detected above 5 sigma is presented.

Using our deeper 20cm survey of the same field, we calculate spectral indices for sources detected in both surveys. For weaker sources, below the detection limit for individual sources at 90cm, we use stacking to study the radio spectra. We find that the spectral indices of small ($< 3''$) 20cm-selected sources with $S_{20} < 10$ mJy have mean and median $\alpha_{20}^{90} \sim 0.3 - 0.5$, where $S \propto \nu^{-\alpha}$. This is flatter than the spectral indices of the stronger source population. At the low end of the 20cm survey, the spectral indices appear to be steepening again. The $\log N - \log S$ counts at 90cm also flatten below 5 mJy. Given the median redshift of the population, $z \sim 1$, the spectral flattening and the flattening of the $\log N - \log S$ counts occurs at radio luminosities normally associated with AGN rather than with galaxies dominated by star-formation.

Subject headings: cosmology: observations — galaxies: evolution — galaxies: starburst — galaxies: active — galaxies

¹National Radio Astronomy Observatory, P. O. Box O, Socorro, NM 87801 USA.; The National Radio Astronomy Observatory is facility of the National Science Foundation operated under cooperative agreement by Associated Universities Inc.

²Institute for Astronomy, University of Hawaii, Honolulu, Hawaii, 96822, USA

³Canada-France-Hawaii Telescope, Kamuela, Hawaii, 96743, USA

⁴Department of Physics & Astronomy, Rutgers University, 136 Frelinghuysen Rd, Piscataway, NJ 08854, USA

1. Introduction

We are building a deep multi-wavelength picture of the sky in the SWIRE Spitzer deep field, 1046+59, which was chosen to be ideal for deep radio imaging. In paper I we discussed the 20cm continuum survey (Owen & Morrison 2008). The present 90cm survey allows us to study the radio spectra of the general source population. For Jansky and mJy sources, very steep radio spectra often are associated with very high redshifts, supposedly due to a combination of the redshifting of the radio spectrum combined with energy losses from synchrotron or inverse Compton radiation. A large population of very steep spectrum, μ Jy sources might suggest a corresponding high redshift μ Jy population. On the other hand, flatter radio spectra are often thought to be connected with synchrotron self-absorption or free-free absorption, although other mechanisms could potentially produce such spectra. Combined with other information the low frequency spectral energy distribution has the potential to give us unique insight on the physics of black-hole-driven AGN and star-forming galaxies. In this paper we report our 90cm observations with the VLA and some analysis of these radio data combined with our 20cm survey of the same field from paper I. In future papers in this series, we will combine these data with redshift measurements and observations at other wavelengths.

2. Observations, Reduction and Cataloging

Observations were made with the VLA in A and C configurations for a total of almost 85 hours on-source between February 2006 and January 2007. However, due to the ongoing EVLA upgrade, only 22 working antennas were typically available in A and 18 in C. Thus the total integration time was equivalent to ~ 63 hours in A and ~ 5 in C, with correspondingly less uv coverage. In Table 1, we summarize the parameters of the observing runs. Since the total time is dominated by the A configuration, the final image for analysis had a resolution $\sim 6''$. The data were all taken in spectral-line mode 4 using on-line Hanning smoothing, resulting in fifteen 390.625 kHz channels in each of 2 IFs (centered at 321.5 and 327.5 MHz) and each of two polarizations. Five second integration times were used in the A configuration and 10 seconds in C. The integration times and channel bandwidths were chosen to minimize tangential and radial smearing of the images away from the field center. This combination of parameters produces the best compromise for imaging sensitivity and quality possible with the current VLA correlator, which dates from the 1970's. The finite bandwidth of the spectral channels still produces some radial smearing of the image away from the field center which we will need to take into account in the analysis of the image. When the EVLA project is completed and the new WIDAR correlator is available, narrower channels, shorter

integration times and a wider total bandwidth should be available for the 90cm wavelength band. So even though no receiver upgrade is planned at 90cm for EVLA, the sensitivity and quality of the imaging should improve.

2.1. Calibration & Editing and Imaging

For calibration, editing, and imaging a procedure similar to the one described in paper I was used. The Baars flux density scale (Baars et al. 1977) was adopted using 3C286 as the flux calibrator. Two of the 15 channels in each IF were deleted due to interference which is generated by the VLA itself and which should disappear when the EVLA is completed. Unless otherwise stated, the AIPS package (Greisen 2003) was used to reduce these data.

A faceted, low resolution image (90" clean beam) with a radius of 15 degrees was made to find interfering sources far from the area of interest. Facets centered on all very bright NVSS sources (> 30 Jy) out to 100 degrees from the field center were also included in this exploratory image. From this search 288 facets, each with 500×500 pixels, were chosen to cover a central region 93' in radius and all the other bright sources found in the low resolution search. The facets were defined using the task SETFC which creates a set of overlapping circular regions within the square facets to cover the entire desired field. Then IMAGR was used to deconvolve all the facets together, using the standard Cotton-Schwab-Clark clean algorithm (Schwab 1984). The cell size for the final image is 2" and the clean beam size is $6.37'' \times 5.90''$ $\text{pa} = 86^\circ$.

Clean images from the first day of the observations were then used as fiducial models for each of the other days. Phase and amplitude calibrations were made of each of the other days using the clean components from the first day images. The A configuration data for each IF and polarization were then combined into a smaller, averaged dataset using STUFFR and images for the full datasets were made. The C configuration data were also calibrated using the full A configuration images. The A and C datasets were then combined using DBCON and images were made separately for each IF and polarization.

After making these images there remained some significant residual structures in the central two degrees of the image due to bright sources located outside the central region. These residuals are likely due to 1) differences in the primary beam patterns from antenna to antenna due to the very simple dipole feeds used on the VLA and 2) the rotation with parallactic angle of the sensitivity pattern on the sky during the synthesis. For bright sources in the outskirts of the field, these variations in sensitivity produce local gain variations which are not taken into account in the imaging and self-calibration process. In order to deal with

this type of error, an AIPS procedure, PEELR, was developed and made generally available in the AIPS package. In PEELR the best clean model is subtracted from the self-calibrated uv data, except for the facet containing the bright source responsible for the residuals. These mostly residual data are then self-calibrated as a function of time using only the model for the bright source. This process allows the variations in gain due the actual primary beam of each antenna to be tracked in time. This local complex calibration is then applied to the mostly residual data and the model for the bright source subtracted from the locally calibrated result. This operation removes, as accurately as possible, the contribution of the offending source. The inverse of the local calibration is applied to the resulting fully residual data and the full clean model added back to the uv database. If there are several offending sources, this process can be repeated for each source as it was in the present case. When the “peeled” dataset is then imaged, the effects of the offending outlying sources are significantly reduced. Techniques like this one have been used by others, but only by combining several different steps and perhaps not quite in the same way as described here.

The resulting images still showed radial smearing for bright sources in excess of what is expected from the finite bandwidths. To explore these errors we subtracted the clean component model from each visibility dataset and made spectral line image cubes from the residual visibilities. For facets containing bright sources far from the field center, these images showed frequency-dependent artifacts which are likely due to the different slopes of the bandpass across each spectral channel. This instrumental problem causes the effective observing frequency for each channel to be slightly different than is assumed and thus the uvw coordinate for each channel used in the imaging to be slightly in error. As a consequence, the source image in each channel is slightly mis-registered, producing a radial smearing for very bright sources far from the field center. To remove the error pattern due to this effect we cleaned the spectral residual image cubes in facets containing bright, outlying sources and subtracted the resulting clean components from the corresponding visibility data. This reduced the error pattern significantly.

The resulting four sets of 288 facets were then made into single images using FLATN. Finally a weighted average of the four images was made, weighting by the $1/\text{rms}^2$, as determined from the IMEAN fit to the pixel histogram. This final image still showed a weak, large-scale error pattern due to the imperfections of the corrections described above. For the final image used for most of the analysis, the AIPS program MWFLT was used to calculate the “mode” of the image over an $82'' \times 82''$ support window and the result was subtracted from the image. For sources approaching this scale size the image before MWFLT was used for analysis but for the vast majority of the sources the MWFLT image was used.

The rms noise near the center of the final image is $\sim 70\mu\text{Jy beam}^{-1}$ which is the

most sensitive image to date made at such a long wavelength. The corresponding value for the 20cm image discussed in paper I is much lower, $\sim 2.7\mu\text{Jy beam}^{-1}$. For a spectral index, $\alpha_{20}^{90} \sim 0.7$ the ratio of flux densities between 90cm and 20cm is ~ 2.8 . Thus the effective sensitivity difference in the field center is about one order of magnitude. However the resolution for the full sensitivity image is about $4\times$ worse at 90cm than at 20cm. Also the primary beam at 90cm about $4\times$ larger. Since many of the sources are resolved at 20cm and most are more than a few arcminutes from the field center, the sensitivity difference is not as large as at the field center and can be better at 90cm than at 20cm very far from the field center. Thus in comparing the two surveys we need to keep in mind the local properties of each source in the image of interest at each wavelength.

2.2. Cataloging

Although the primary beam has a diameter of 2.3° and the region we imaged extends out far beyond this limit, we chose to catalog the region within 1° of the field center. This two-degree diameter field-of-view covers more than the entire field we are studying at other wavelengths. Moreover, the primary beam shape becomes less well known beyond one degree and the smearing due to the finite channel width begins to become important beyond this radius. As with the 20cm survey we include the radial smearing due to the finite bandwidth in our Gaussian fits. In the present case the radial smearing is approximately $0.0012\times$ (the distance from the field center) in arcseconds. In the worst case, for a point source at the maximum cataloged radius from the field center, this bandwidth smearing amounts to a decrease in the peak brightness at full resolution of $\sim 18\%$. As for the 20cm survey, we convolved our $\sim 6''$ images to resolutions of $12''$ and $24''$ to increase the detection sensitivity for large sources. This exercise was much less important than it was for the 20cm survey, but it did yield higher S/N detections for a subset of the survey.

As for the 20cm survey, the AIPS program SAD was used for forming the initial source lists. A catalog for each resolution was formed down to a peak signal/noise (S/N) of 4.5. The residual images from SAD were then searched to find any remaining sources missed by the program with a S/N greater than 5.0. For sources with a S/N close to 5.0, the fitting process was repeated by hand with JMFIT, using the local rms estimate over a region 100 pixels in diameter. In this way a reliable list of sources with S/N of 5.0 or greater at each resolution was compiled. For both SAD and JMFIT, the smearing due to the finite bandwidth was included in the fitting process. As described for the 20cm survey in paper I, the best description of each of the sources with a peak $S/N \geq 5$ at one of the resolutions analyzed was included in the final 90cm catalog. In order to allow for a variety of potential

calibration errors, a 3% noise term proportional to the total measured flux density of each source was folded into the errors in quadrature, as was done for the 20cm survey.

3. Results

3.1. Radio Catalog

In Table 2, we give the first ten lines of the radio catalog; the full table is provided electronically. Column (1) contains the source number. If the source has a number less than 3000, then it was found with a $S/N \geq 5.0$ from running SAD on the full resolution image. Sources with numbers ≥ 10000 were found in lower resolution images or in checks of the residual images. Numbers beginning with 12 were measured on a $12''$ resolution image. If the number begins with 24 then we used a $24''$ resolution image. Columns (2) and (3) contain the radio RA and Dec along with the estimated error. Column (4) contains the corrected peak flux density from the map in μJy per beam. In column (5) we list the corrected total flux density. In column (6) we give the estimated error in the total flux density. Column (7) contains the peak S/N. The error for column (4) can be recovered by dividing column (4) by column (7). We give the S/N as opposed to the error since the S/N was used to define the catalog cutoff and later is used in the calculation of $\log N - \log S$. In column (8), we give the best fit deconvolved size in arcseconds. If a resolved two dimensional Gaussian was the best fit, we give the major and minor axis size (FWHM) and the position angle. Upper limits are given for sources which were unresolved based on the results of JMFIT or SAD. For sources with very large sizes, for which only a largest angular size is given in column (8), sizes and total flux densities were estimated directly from the images using the AIPS routines, IMVAL and TVSTAT.

3.2. Angular size distribution

The 90cm catalog covers a larger area than the 20cm survey but at a lower sensitivity. This means that the 90cm survey samples a higher range in apparent flux density with different properties in angular size and absolute radio luminosity. In Figure 1 we show the median angular size – 90cm flux density distribution. Above 3 mJy we resolve most of the sources but below 3mJy most of the sources are relatively small. This trend in the median sizes is shown in Table 3 and Figure 2. Although similar resolution data have not been reported at 90cm, these results are consistent with previous results at higher frequencies, extrapolated to 90cm (Windhorst 2003).

Some of the 90cm sources have larger sizes than the corresponding 20cm counterparts. For these sources we checked the flux densities and sizes at 20cm by smoothing to the resolution of the 90cm detection images. For most of these sources the lower resolution 20cm sizes and flux densities agree well with the fits at the original resolution. The total flux density changed by more than 10% for only three individually cataloged 20cm sources (00061, 01186 and 01193). In making the 20cm catalog, the larger flux densities at lower resolution were rejected because the S/N was significantly higher on higher resolution images which fitted smaller sizes. The 90cm survey is also more sensitive to smaller spatial frequencies and any steeper spectrum, more extended emission. While these results do not change any of the conclusions in paper I, we are likely a little incomplete for the largest sources, especially near the bottom of the catalog. For the spectral index analysis below we have used the 20cm fits from imaging at 90cm resolution.

3.3. Spectral Indices

3.3.1. 90cm selected sources

For our spectral index analysis we will restrict ourselves to sources within $20'$ of the field center. At that radius we are complete at 20cm and beyond that distance from the field center the uncertainty due to the primary beam correction at 20cm becomes significant. Since the 20cm image is so deep, almost all the 90cm sources within $20'$ of the field center have counterparts which we can use to determine spectral indices. Two 90cm sources (01492 and 01501) were detected on the 20cm $6''$ resolution image only with $S/N < 5$. Three more sources (00766 $\alpha > 1.46$, 01346 $\alpha > 1.71$ and 01491 $\alpha > 1.84$) have no 20cm counterpart with a $S/N > 3$. However, these three sources all have low S/N detections, $5.0 < S/N < 5.6$, and have no counterparts on our deep optical/NIR images (Strazzullo et al. 2009) or our deep 50cm GMRT image (Owen et al. 2009). These sources either have very steep spectra and are very distant sources or they are spurious. We choose to leave them out of the following discussion but note that there may be a small, very steep spectrum tail to the distribution. In Table 4 we give the first ten lines of the electronic table summarizing the 90cm-selected spectral indices.

Figure 3 contains the observed histogram of 90 to 20cm spectral indices ($S \propto \nu^{-\alpha}$) for sources detected above 5 sigma at 90cm. In Table 5 we summarize the statistics for these sources as a function of 90cm flux density and size. The mean and median spectral indices are ~ 0.7 for all of our subsets. This value is flatter than the mean 408-1407 MHz spectral index of 0.92 from 5C12 for sources detected at 408 MHz above 40 mJy (Benn et al. 1982). We have only a few sources with 90cm flux densities > 40 mJy in our 90cm survey,

so our results are consistent with a flattening in the mean spectral index below the 5C12 characteristic flux density. The deeper LBDS 327 MHz survey has a 90cm-selected, 327-1462 MHz median spectral index shifting from ~ 0.9 above 100 mJy, to ~ 0.7 between 10 and 100 mJy, and then down to ~ 0.5 between 3.6 and 10 mJy (Oort et al. 1988). We agree with their estimate in the 10 – 100 mJy range but do not find the flatter median spectral index below 10 mJy near the bottom of the LBDS survey.

3.3.2. 20cm selected sources

Most recent work on deep fields involves surveys at 20cm, so it is also interesting to study the spectral index distribution selecting the sources at 20cm. Since most of the 20cm sources are not detected directly at 90cm, we must use a combination of a high 20cm flux density cutoff to study the stronger 20cm sources individually and stacking subsets at 90cm in order to study the fainter 20cm population. Most of the weaker sources are much smaller than the size of the synthesized beam of our 90cm survey (see paper I). Those sources that are expected to be unresolved at 90cm are suitable for stacking analysis.

For the high flux density subset, we select only 20cm sources with total flux densities $> 100\mu\text{Jy}$ from paper I within $20'$ of the field center. In Table 6 we show the first 10 lines of the electronic table of the 90cm–20cm spectral indices for these sources. In Figure 4 we plot the histogram of the spectral indices of these sources against their 20cm flux densities. Since, in this subset of sources, many of the sources are not detected above 3 sigma at 90cm, we plot the blue area for sources detected above 3 sigma while the red area represents the 3 sigma upper limit corrected for the observed 20cm source size. The median spectral index is 0.52(0.04) including the upper limits, significantly flatter than the 90cm selected sample and samples with brighter limiting flux densities selected at 20cm. In Figure 5 we show spectral index plotted against the 20cm flux density for sources with $S_{20} > 100\mu\text{Jy}$. This plot shows the sources with 90cm upper limits as red circles clearly delineating the section of the plot which is not allowed due to the 90cm sensitivity. Even with this high limit on the 20cm catalog, 37% of the sources with $100\mu\text{Jy} < S_{20} < 1000\mu\text{Jy}$ have upper limits at 90cm; thus we cannot determine the details of the dependence of the spectral index distribution on 20cm flux density for $S_{20} < 1$ mJy from the properties of individual sources.

In order to study the spectral index distribution down to the bottom of the 20cm catalog, we need to use stacking on the 90cm image. Since we need to restrict the stacks to angular sizes which are effectively unresolved, we omit a modest, but significant number of sources that are resolved by the 90cm synthesized beam. In the following discussion, we divide the sources into subsets by ranges of 20cm flux density and also split the subsets into sources

which are $> 3''$ and $\leq 3''$. In Paper I we found that sources with $S_{20} < 1$ mJy have a median size of $\sim 1''$, unlike the stronger sources individually detected at 90cm. If we omit from the stacking analysis the $\sim 10\%$ of sources with $S_{20} < 1$ mJy that have sizes $> 3''$, we expect that the spectral properties of the $\leq 3''$ subsets should be close to those of the full population. In stacking each subsample with flux densities at 20cm < 1 mJy, we extract the observed 90cm brightness in $\mu\text{Jy}/\text{beam}$ at the position of the 20cm source. For small sources this should be a good estimate of the total flux density in μJy . Within the subset, we then calculate the mean and median flux densities at both frequencies. The spectral index computed from the two mean flux densities and that computed from the two median flux densities are listed for each subset in the bottom six lines of Table 7. The errors in Table 7 are calculated assuming counting statistics from the total number in each subset, combined in quadrature with an assumed standard deviation for the population of spectral indices of 0.30 which seems appropriate based on the higher flux density, 90cm-selected, spectral indices but is only an educated guess.

For sources stronger than 1 mJy at 20cm, all except one have a detection at 90cm. Excluding this source we can calculate the median and mean spectral index for subsets selected by source flux density and size and these are listed in Table 7. In Figure 6 we summarize the results graphically. Above 1 mJy, where we can study both size subsets, the more resolved sources have steeper spectra than the $\leq 3''$ subset. The mean and median spectral indices continue to flatten for the full population. For the small sources, the median and mean spectral indices flatten to $\sim 0.3 - 0.5$. Below 1 mJy the small source medians and means continue to be in the range $\sim 0.3 - 0.5$, but with a clear trend to steeper spectra at the lowest flux densities in the 20cm sample.

3.3.3. 90cm versus 20cm selection

Thus the results for the spectral indices are quite different depending on whether we select the samples at 90cm or 20cm. At 90cm we find very constant mean and median spectral index of ~ 0.7 down to the survey limit of $300\mu\text{Jy}$. No obvious dependence is found on angular size. Approximately the same result is found in the 90cm selected sample down to 1 mJy at 20cm which would correspond to ~ 3 mJy at 90cm with a spectral index ~ 0.7 . However, sources $> 3''$ in size tend to have steeper spectra than those $\leq 3''$. Below 1 mJy at 20cm, many more sources do not have detections than would be expected if the ~ 0.7 spectral index continued. For these and weaker sources, we are forced to consider only small sources since the surface brightness sensitivity at 90cm is not high enough to detect sources of all angular sizes. For this population of small sources, we find much flatter median and

mean spectral indices, $\sim 0.3 - 0.5$. This result suggests that there is a smaller size, 20cm source population which is attenuated enough at 90cm, relative to an $\alpha_{20}^{90} \sim 0.7$, to affect the median source properties relative to a 90cm-selected population.

3.4. Log N - Log S

The calculation of the 90cm log N - log S is much easier than for 20cm in paper I because 1) we only consider a radius of one degree which doesn't reach the half power point of the primary beam and 2) the synthesized beam is bigger, $\sim 6.2''$ so fewer sources are resolved, and 3) the fractional channel bandwidth is smaller. These parameters dramatically reduce the problems we faced in paper I and allows us to perform a simpler analysis. Only below 1 mJy is the incompleteness due to source size an issue. For these weak sources we use the same formalism as in paper I to account for missing sources due to resolution and bandwidth smearing and the same assumed source size distribution. Even for these weaker sources, since the resolution is lower, the impact of these corrections is very small. In Table 8, we summarize our results for the 5 sigma catalog only, unlike paper I where we performed a more complicated calculation with a variable S/N cutoff.

In Figure 7, we plot our results along with the 327 MHz results for LBDS (Oort et al. 1988) for their 5 sigma catalog and the 5C12 results from 408 MHz scaled by their quoted mean spectral index of 0.9 to 324.5 MHz (Benn et al. 1982). The results are in general agreement and our additions show that we have reached the flat region of the counts seen at other frequencies near 3 mJy. This change in slope also corresponds roughly to the minimum in the spectral index distribution seen in Figure 6.

4. Discussion

These data fill out the picture of the meter-wavelength radio sky a bit more clearly, building on the earlier work cited above, but also raise new questions. Instead of finding a large steep spectrum population, we find flatter spectra for the subset of sources with ($< 3''$) and $S_{20} < 10\text{mJy}$. We also find that the differential log N - Log S at 90cm flattens in roughly the same flux density range ($S_{90} < 5\text{mJy}$). Thus the nature of the meter wavelength population seems to be changing in the few mJy range. Often a trend toward flattening radio spectra at higher frequencies and the corresponding change in slope of log N - log S is attributed to star-forming galaxies becoming dominant (e.g., Windhorst 2003). However, only for 20cm luminosities $< 10^{23}\text{ W Hz}^{-1}$ are star-forming galaxies more common than

AGN (e.g., Condon et al. 2002). For sources with $S_{20} > 1\text{mJy}$ (equivalent to $S_{90} > 2\text{mJy}$ with $\alpha_{20}^{90} \sim 0.5$) to have a 20cm luminosity $< 10^{23} \text{ W Hz}^{-1}$, their redshift would have to be < 0.2 . This redshift is much too low for most such mJy sources to be dominated by star-formation, since we find a median $z \sim 1$ for our sample (Strazzullo et al. 2009). Thus it seems likely that the changes we are observing are in the AGN population. Furthermore, spectral studies at wavelengths $< 20\text{cm}$, show that the typical μJy source has a quite steep spectrum, $\sim 0.8 - 0.9$ (Fomalont et al. 2006). Therefore our 20cm-selected μJy sources with flatter spectra cannot be due to free-free emission, since the flat spectrum free-free emission should be less important at longer wavelengths.

One might think that flatter spectra in AGN might be due to synchrotron self-absorption as is seen in many beamed radio galaxies and quasars. However, our work in paper I and other studies (e.g., Muxlow et al. 2005; Fomalont et al. 2006) show that the typical sizes for these sources are $\sim 1''$. This argues against synchrotron self-absorption being dominant since that mechanism requires sizes $\ll 1$ milliarcsecond to be important. One possibility is that the flatter spectra could result from the combination of a relatively flat AGN jet with a spectral index ~ 0.5 (e.g., Bridle & Perley 1984; Butcher et al. 1980) with a synchrotron self-absorbed core.

Since the sources are relatively small, free-free absorption is a possibility. Free-free absorption for such sources depends in general on the details of the clumpiness of the absorbing thermal gas and its geometric relation to the synchrotron emitting medium. In star-forming systems which have been well studied, the radio emission is extended more uniformly throughout the galaxy than the dust or the HII regions (Hoernes et al. 1998; Murphy et al. 2008). Free-free absorption is also seen on small scales in some radio AGN (e.g., Walker et al. 1994; Gallimore et al. 2004). For a uniform density foreground medium with a temperature $\sim 10^4\text{K}$, the characteristic free-free absorption turnover frequency is $\nu_t(\text{MHz}) \sim 0.5n(\text{cm}^{-3})l^{0.5}(\text{pc})$, where l is the projected pathlength. For example, for a typical source in our sample with a size of $1''$ at $z \sim 1$, a typical radius is $\sim 4 \text{ kpc}$ and, for a rest frame turnover frequency of $\sim 300 \text{ MHz}$, one needs a density of 10 cm^{-3} , which would correspond to a mass of $\sim 6 \times 10^{10} M_{\odot}$ if uniformly distributed in a sphere. A more realistic model with a smaller filling factor and a different geometry reduces the mass estimates but if free-free absorption is important then a reasonably large mass of ionized gas must be involved. The flattening could also be due to ionization losses as has been suggested for some star-forming galaxies (e.g., Thompson et al. 2006). In any case, the flatter spectra and the flatter counts observed below 3 mJy suggest a change in the nature of the population below this flux density level which is not well understood. We will discuss this point further in future papers where we add redshifts and data from other wavelengths to the analysis.

5. Conclusion

We have presented the most sensitive 90cm image to date of the SWIRE deep field. This image combined with our uniquely sensitive 20cm image of this field allows us to study the meter wavelength spectral indices as a function of flux density for the μJy radio population. For the subset of sources selected at 20cm with sizes $< 3''$ (which contains about $\sim 90\%$ of all 20cm-selected sources $< 1 \text{ mJy}$), the mean and median spectral indices flatten from $\alpha \sim 0.7$ to $\alpha \sim 0.3 - 0.5$ below 10 mJy with a trend toward steeper spectra at the lowest flux densities. The 90cm log N-log S counts flatten below 3 mJy as they do at corresponding low flux densities at higher frequencies. The change in the source properties at a few mJy is not well understood but probably involves the AGN population, not primarily star-formation-dominated galaxies.

REFERENCES

- Baars, J. W. M., Genzel, R., Pauliny-Toth, I. I. K., & Witzel, A. 1977, *A&A*, 61, 99.
- Benn, C. R., Grueff, G., Vigotti, M. & Wall, J. V. 1982, *MNRAS*, 200, 747.
- Bridle, A. H., & Perley, R. A. *ARA&A*, 22, 319.
- Butcher, H. R., van Breugel, W. & Miley, G. K. 1980, *ApJ*, 235, 749.
- Condon, J. J., Cotton, W. D. & Broderick, J. J. 2002, *AJ*, 124, 675.
- Fomalont, E. B., Kellermann, K. I., Cowie, L. L., Capak, P., Barger, A. J., Partridge, R. B., Windhorst, R. A. & Richards, E. A. 2006, *ApJS*, 167, 103.
- Gallimore, J. F., Baum, S. A. & O’Dea, C. P. 2004, *ApJ*, 613, 794.
- Greisen, E. W. 2003, in *Information Handling in Astronomy – Historical Vistas* (ed. A. Heck), Kluwer, Dordrecht, 109.
- Hoernes, P. Berkhuijsen, E.M., & Xu, C. 1998, *A&A*, 34, 57.
- Murphy, E. J., Helou, G., Kenney, J. D. P., Armus, L., & Braun, R. 2008, *ApJ*, 678, 828.
- Muxlow, T. W. B., Richards, A. M. S., Garrington, S. T., Wilkinson, P. N., Anderson, B., Richards, E. A., Axon, D. J., Fomalont, E. B., Kellermann, K. I., Partridge, R. B., & Windhorst, R. A, 2005, *MNRAS*, 358, 1159.
- Oort, M J. A., Steemers, W. J. G. & Windhorst, R. A. 1988, *A&AS*, 73, 103.
- Owen, F. N. & Morrison, G. E. 2008 *AJ*, 136, 1889 (paper I).
- Owen et al. 2009 (in preparation).
- Schwab, F. R. 1984, *AJ*, 89, 1076.
- Thompson, T. A., Quataert, E., Waxman, E., Murray, N., & Martin, C. L. 2006, *ApJ*, 645, 186.
- Strazzullo et al 2009 (in preparation).
- Walker, R. C., Romney, J. D. & Benson, J. M. 1994, *ApJ*, 430, L45.
- Windhorst 2003, *New A Rev.*, 47, 357.

Table 1. Observing Runs Summary

Configuration	Startdate	Enddate	Hours
A	06Feb19	06May17	77.1
C	07Jan04	07Jan05	7.9

Table 2. Radio Source Catalog

Name	RA(2000.0)	Dec(2000.0)	Peak $\mu\text{Jy}/\text{b}$	Total μJy	Error μJy	S/N	Size " x" pa= $^{\circ}$
00018	10 38 14.59(0.03)	59 02 36.0(0.1)	2778	5425	320	26.7	12x2pa= 91
00033	10 38 24.54(0.05)	59 00 34.2(0.3)	1302	1510	206	11.7	5x0pa=54
12017	10 38 24.64(0.10)	59 00 35.1(0.6)	1423	2498	340	10.9	15x6pa=64
00036	10 38 25.64(0.11)	59 05 58.0(0.5)	620	892	241	5.5	8x0pa=113
00043	10 38 29.75(0.03)	58 52 05.0(0.2)	1071	1071	115	9.7	<3
12045	10 38 31.50(0.03)	58 47 09.0(0.4)	3024	4763	348	22.2	14x3pa=13
00051	10 38 34.56(0.07)	59 15 15.3(0.5)	629	629	116	5.5	<6
00058	10 38 37.82(0.01)	59 09 45.2(0.1)	5423	5423	196	49.8	<2
00059	10 38 39.16(0.01)	58 59 12.3(0.1)	28469	28570	874	271.1	<2
00065	10 38 42.27(0.05)	59 01 10.5(0.3)	919	919	118	8.0	<4

Table 3. 90cm Source Size Statistics

$\log(S_{90})$ μJy	Num ^a	Size ^b "	$\log(S_{90}^c)$ μJy
5.0 – 6.1	20	17.0(7.9)	5.25
4.0 – 5.0	95	7.0(4.5)	4.41
3.5 – 4.0	126	4.5(2.7)	3.71
3.0 – 3.5	335	< 4	3.18
2.5 – 3.0	859	< 5	2.76

^aNumber of sources in interval.

^bMedian size with error in median in parenthesis.

^cMedian 90cm flux density

Table 4. Spectral Indices for 90cm Selected Sources

Name	α_{20}^{90a}	Error	S_{90}	S_{20}	Res ^b	Size	Res ^b	Size
90cm		α_{20}^{90}	μJy	μJy	90cm	"	20cm	"
00725	0.57	0.07	758	330.2	<	4	r	2.6
00727	0.48	0.11	813	211.4	r	7	<	2.4
00728	-0.40	0.04	1616	2906.2	<	3	r	1.5
00733	0.29	0.04	1219	803.6	<	1	r	0.8
00737	0.48	0.04	3000	1487.5	r	2	r	2.0
12407	0.90	0.06	1211	272.4	r	12	r	7.0
00744	0.72	0.12	390	136.3	<	6	r	2.8
00755	0.46	0.06	2090	1069.1	r	9	r	8.3
00756	0.86	0.12	402	114.4	<	5	<	2.4
00761	0.33	0.09	512	314.3	<	3	r	1.3

^a90cm-20cm spectral index, $S \propto \nu^{-\alpha}$

^b'<': next column upper limit, 'r': next column deconvolved major axis

Table 5. Spectral Index Summary for 90cm Selected Sources

$\log(S_{90}^a)$ μJy	Num ^b	α^c mean	α^c med	std ^d dev	$\log(S_{90}^e)$ mean	$\log(S_{90}^e)$ med
All						
2.5 – 5.0	229	0.68(0.02)	0.70(0.03)	0.31	3.38	2.77
4.0 – 5.0	11	0.70(0.05)	0.66(0.07)	0.17	4.48	4.37
3.0 – 4.0	56	0.68(0.04)	0.76(0.06)	0.34	3.37	3.23
2.5 – 3.0	162	0.68(0.02)	0.70(0.03)	0.30	2.72	2.67
> 3''						
2.5 – 5.0	55	0.71(0.03)	0.72(0.04)	0.21	3.68	3.02
4.0 – 5.0	7	0.75(0.08)	0.77(0.10)	0.19	4.43	4.24
3.0 – 4.0	22	0.74(0.05)	0.76(0.07)	0.24	3.40	3.25
2.5 – 3.0	26	0.68(0.04)	0.67(0.05)	0.19	2.77	2.76
≤ 3''						
2.5 – 5.0	174	0.67(0.03)	0.70(0.03)	0.34	3.22	2.70
4.0 – 5.0	4	0.60(0.04)	0.61(0.05)	0.06	4.54	4.49
3.0 – 4.0	34	0.65(0.07)	0.67(0.08)	0.38	3.37	3.23
2.5 – 3.0	136	0.68(0.03)	0.71(0.04)	0.19	2.77	2.77

^aRange of the log of 90cm flux densities in the interval.

^bNumber of Sources in the interval.

^cSpectral Index between 90cm and 20cm defined as ($S \propto \nu^{-\alpha}$).

^dEstimated standard deviation in the population

^e μJy

Table 6. Spectral Indices for 20cm Selected Sources

Name 20cm	α_{20}^{90a}	Error α_{20}^{90}
00013	0.57	0.07
00016	-0.40	0.04
00021	1.02	0.06
00024	0.58	0.18
00028	0.86	0.12
00029	0.33	0.09
00030	0.82	0.10
00033	<0.28	
00037	<-0.12	
00044	-0.64	0.10

^a90cm-20cm spectral
index, $S \propto \nu^{-\alpha}$

Table 7. 20cm Selected Spectral Index Summary

$\log(S_{20}^a)$ μJy	Num ^b	α^c mean	α^c med	$\log(S_{20}^d)$ mean	$\log(S_{20}^d)$ med
All					
2.5 – 5.0	269		0.52(0.04)		
3.0 – 5.0	24	0.58(0.09)	0.66(0.11)	3.73	3.40
4.0 – 5.0	5	0.75(0.15)	0.66(0.19)	4.21	4.16
3.0 – 4.0	19	0.54(0.11)	0.66(0.27)	4.22	4.15
> 3"					
3.0 – 5.0	12	0.75(0.10)	0.76(0.12)	3.71	3.57
4.0 – 5.0	2	0.93(0.30)	0.93(0.36)	4.19	4.19
3.0 – 4.0	10	0.71(0.11)	0.74(0.14)	3.49	3.44
≤ 3"					
3.0 – 5.0	12	0.42(0.14)	0.60(0.17)	3.75	3.35
4.0 – 5.0	3	0.62(0.15)	0.57(0.19)	4.19	4.16
3.0 – 4.0	9	0.35(0.18)	0.59(0.22)	3.28	3.29
2.5 – 3.0	28	0.47(0.07)	0.30(0.09)	2.69	2.70
2.3 – 2.5	35	0.38(0.06)	0.37(0.08)	2.41	2.41
2.1 – 2.3	87	0.49(0.05)	0.45(0.06)	2.20	2.20
1.9 – 2.1	180	0.48(0.04)	0.50(0.05)	2.00	2.00
1.6 – 1.9	485	0.50(0.04)	0.52(0.05)	1.74	1.74
1.0 – 1.6	479	0.59(0.04)	0.52(0.05)	1.46	1.46

^aRange of the log of 20cm flux densities in the interval.

^bNumber of Sources in the interval.

^cSpectral Index between 90m and 20cm defined as ($S \propto \nu^{-\alpha}$).

^d μJy

Table 8. Differential normalized source counts for 1046+59. The table contains 1) S_l (the lower flux density limit of the bin), 2) S_h (the upper flux density limit of the bin), 3) the normalization factor and its error.

S_l μJy	S_h μJy	$S^{2.5}dN/DS$ $\text{Jy}^{1.5}\text{sr}^{-1}$
375	475	25.4 ± 3.7
475	600	25.9 ± 3.7
600	900	16.9 ± 1.8
900	1350	17.2 ± 2.4
1350	2000	19.3 ± 2.0
2000	3000	27.3 ± 2.9
3000	4500	30.8 ± 4.2
4500	6750	58.0 ± 7.9
6750	10000	48.7 ± 9.4
10000	20000	89.0 ± 14.7
20000	40000	243.6 ± 43.7
40000	80000	495.6 ± 105.1
80000	160000	398.1 ± 162.5

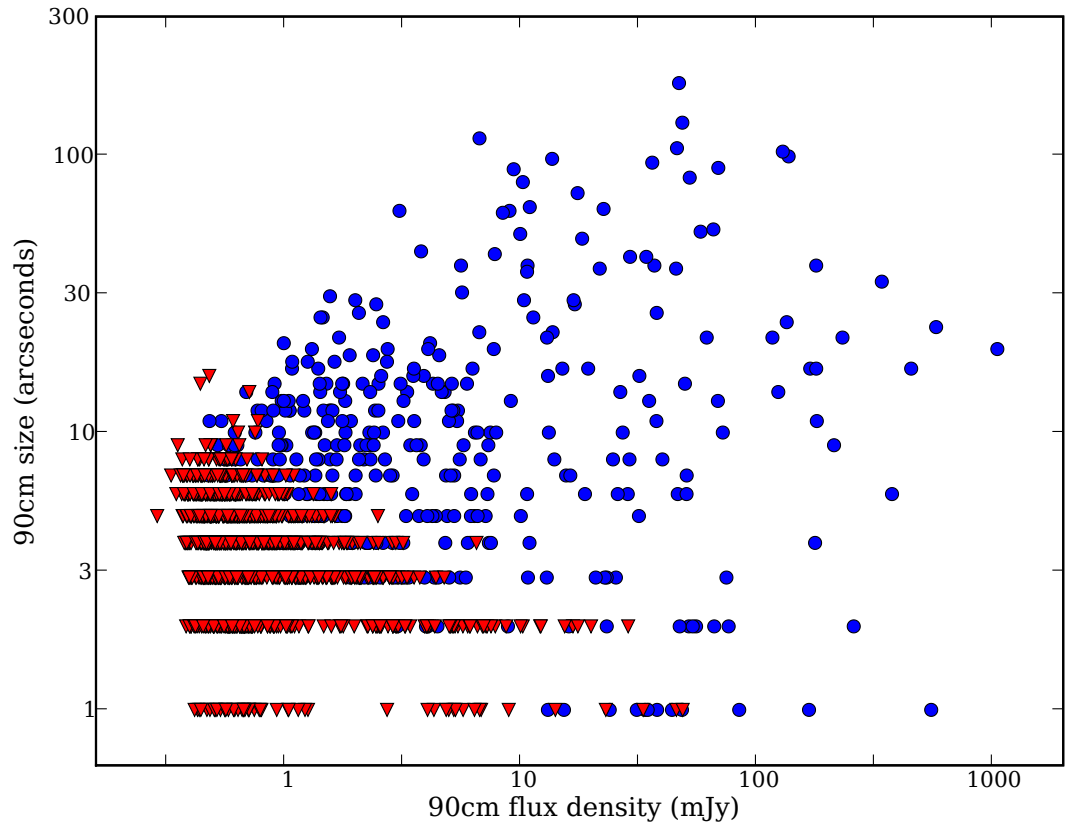


Fig. 1.— Log-Log plot of angular size versus 90cm flux density using the data in Table 2. Blue dots are for significantly resolved sources while the red triangles represent sources with upper limits to the angular size.

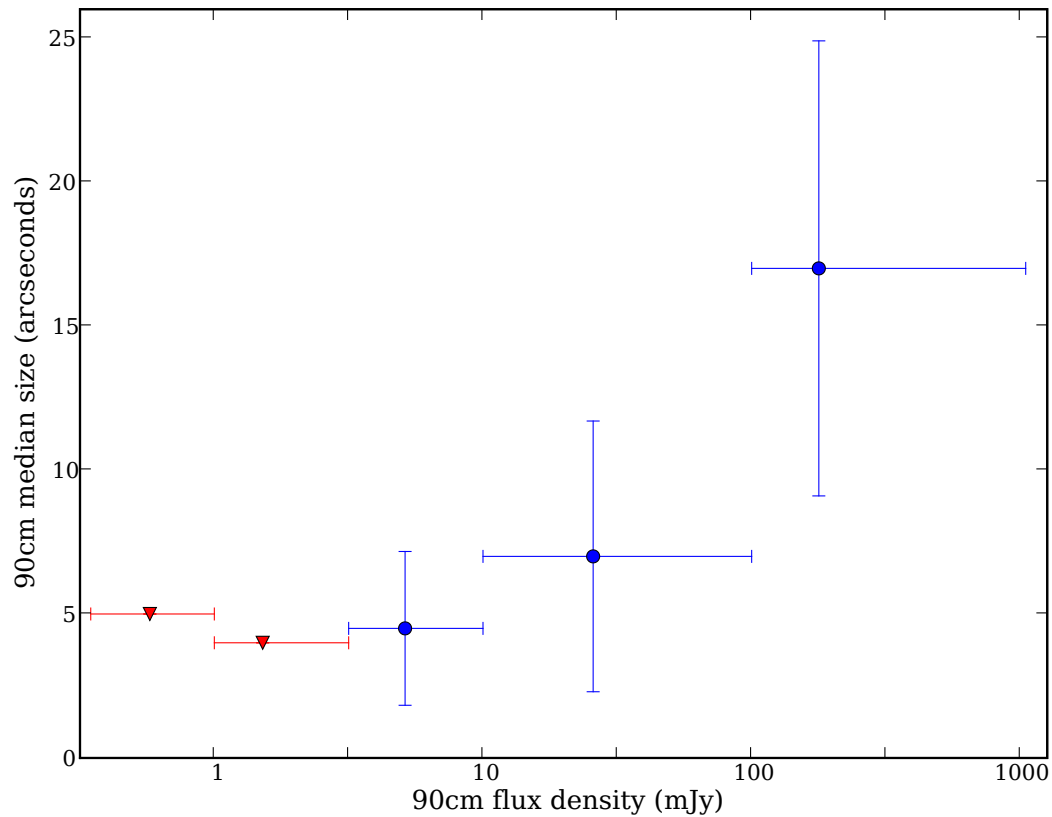


Fig. 2.— Observed median angular size for various different logarithmic ranges in 90cm flux density. Blue dots show significant detections of the median while the red triangles are upper limits to the median. The error bars in the flux densities show the size of the bins used to calculate the statistics, while the error bars in the sizes are estimated error in the median values.

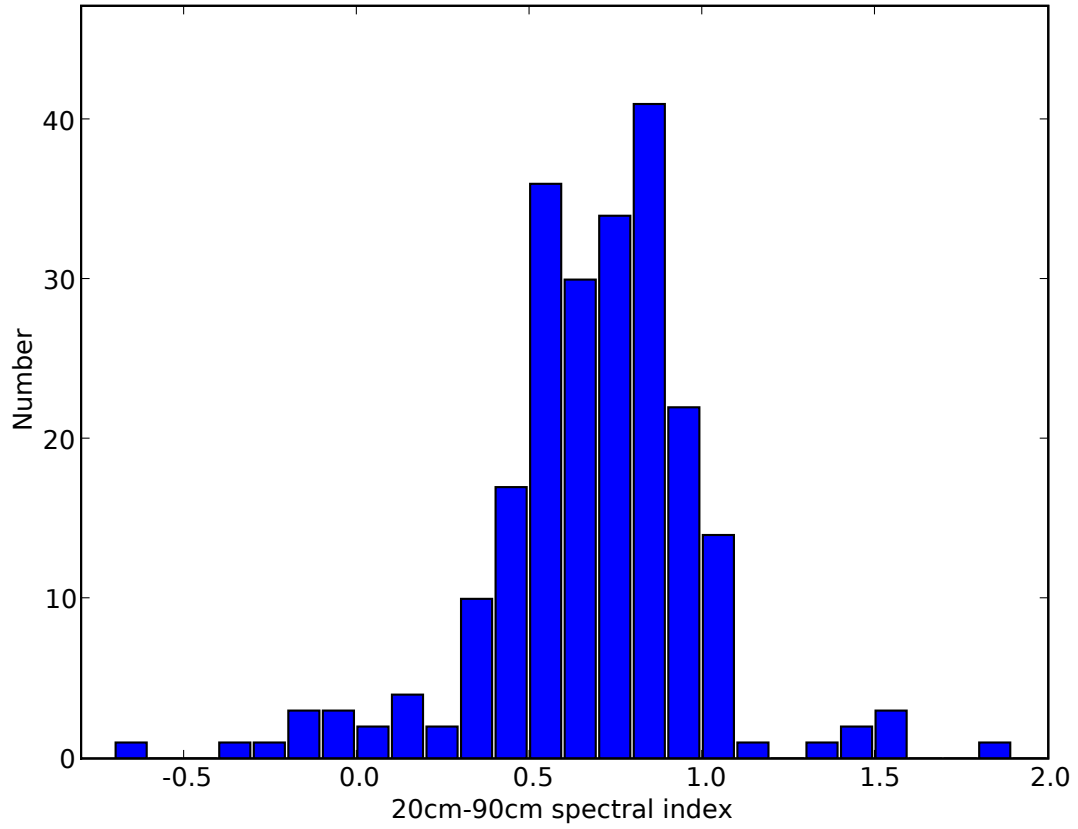


Fig. 3.— Histogram of 90cm to 20cm spectral indices for sources detected above 5 sigma at 90cm in the region cataloged for the 20cm survey.

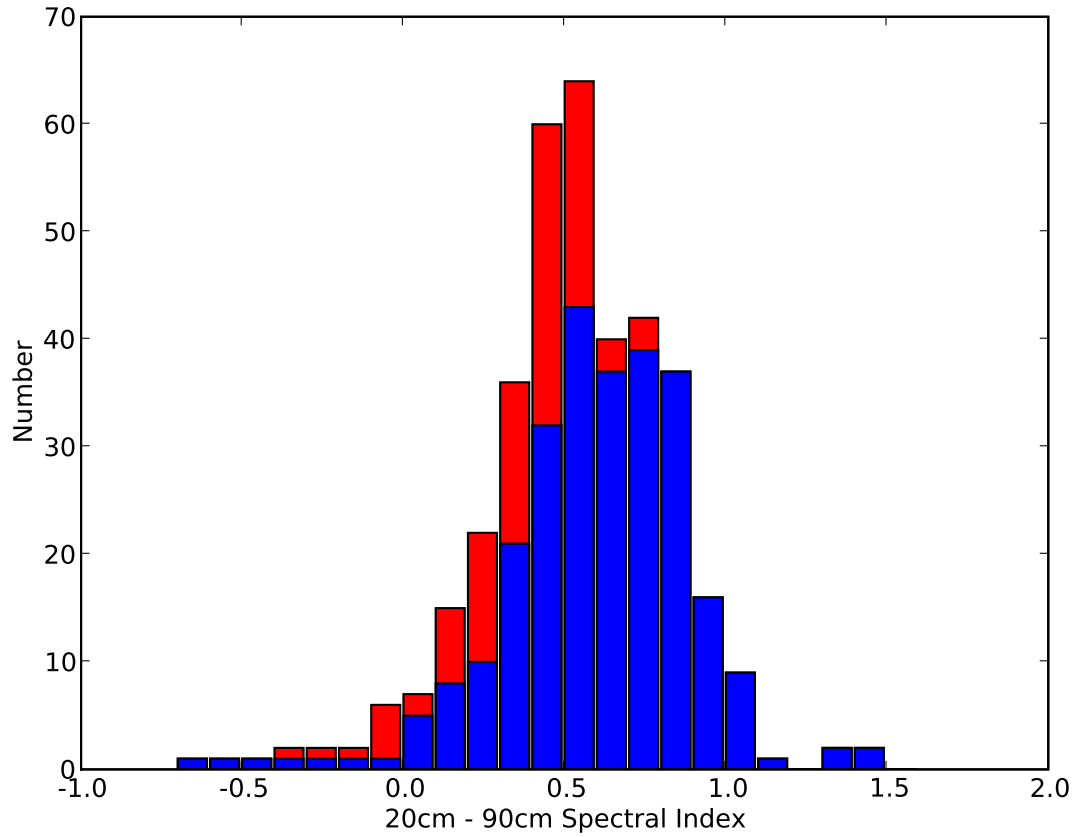


Fig. 4.— Histogram of 90cm to 20cm spectral indices for sources with 20cm flux densities $> 100\mu\text{Jy}$. Blue: measured spectral indices for 90cm sources with $S/N > 3$ sigma, Red: 3 sigma upper limits for 90cm sources with $S/N < 3$ sigma.

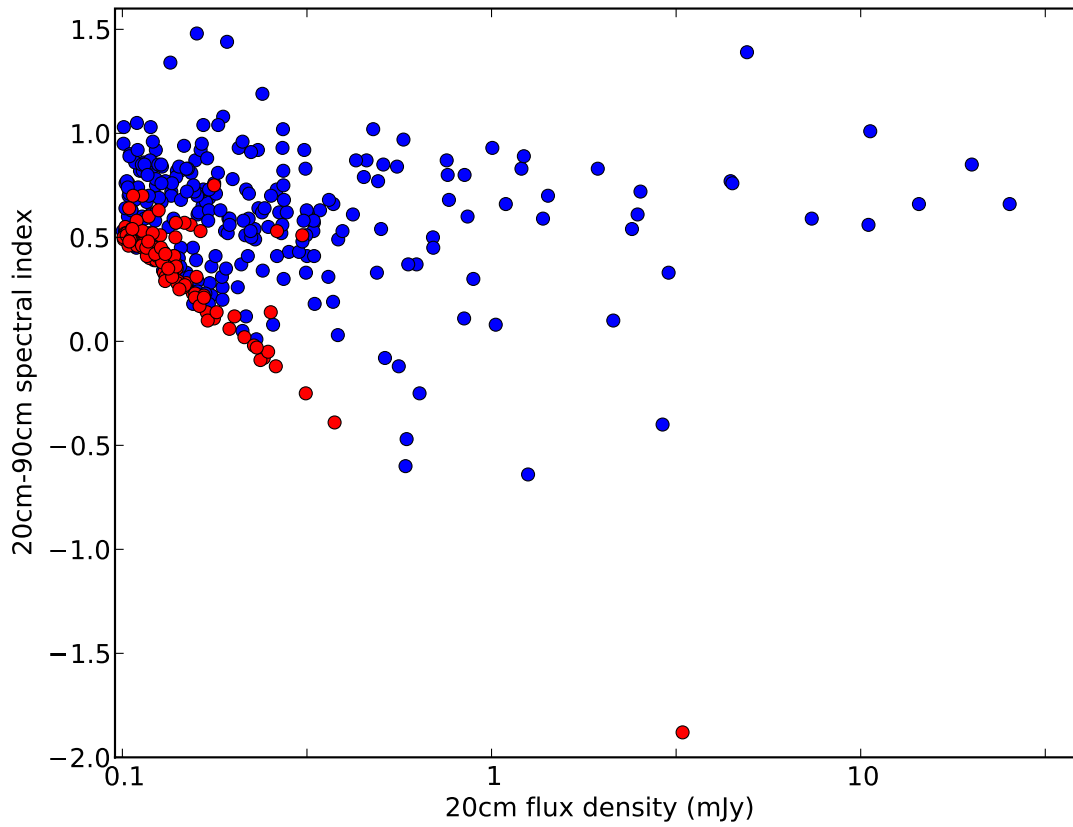


Fig. 5.— 90cm to 20cm spectral indices versus 20cm flux density plotted on a logarithmic scale. Blue dots are sources with 90cm detections > 3 sigma. Red dots are sources with 3 sigma 90cm upper limits.

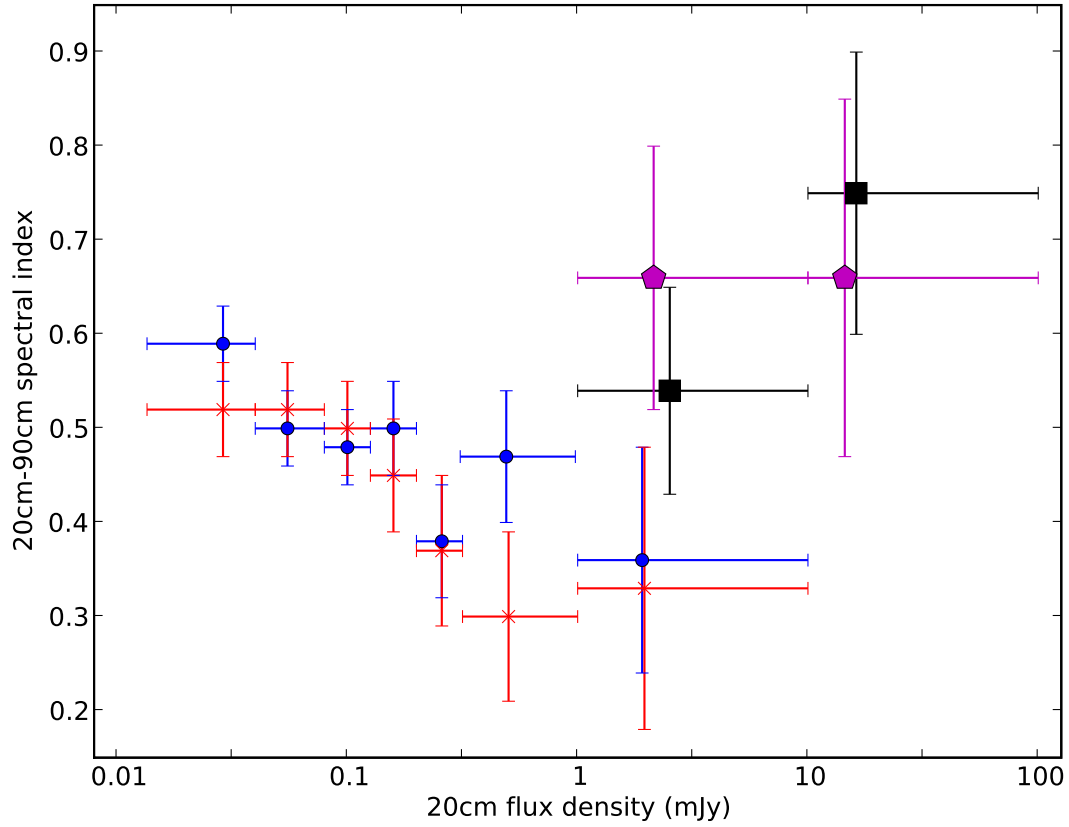


Fig. 6.— 20cm selected spectral index versus 20cm flux density in mJy in various intervals in 20cm flux density: The results are from table 7. The black squares and the magenta pentagons are the means and medians for the entire sample. The blue circles and red crosses are the means and medians for sources with 20cm sizes $\leq 3''$ using stacking of 90cm cutouts as described in the text. The flux density error bars show the sizes of the bins while the spectral index error bars show the estimated error in mean or median.

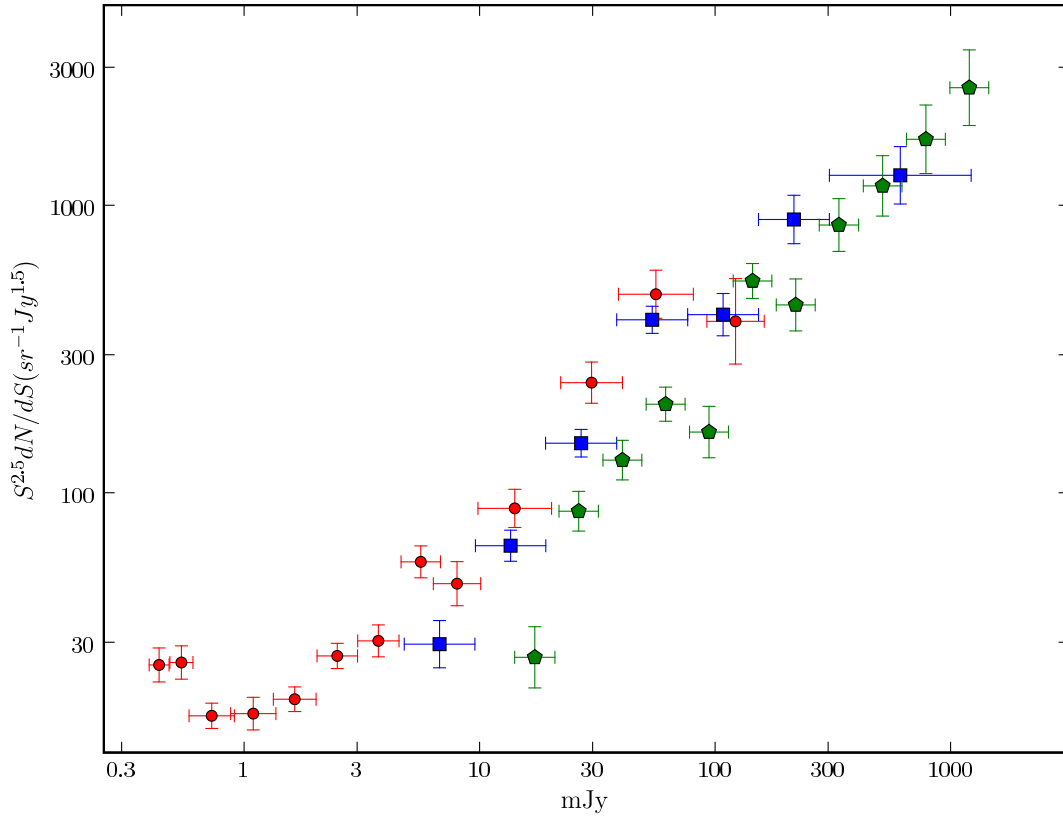


Fig. 7.— 90cm log N – log S differential distribution. Green pentagons are from the 5C12 survey at 408 MHz scaled to 324.5 MHz using a mean spectral index of 0.9 (Benn et al. 1982). Blue squares are from 327 MHz observations with Westerbork of the LBDS (Oort et al. 1988). Red circles are from this paper in table 8.

